

## EVOLUTIONARY SIGNATURES IN THE FORMATION OF LOW-MASS PROTOSTARS

CHADWICK H. YOUNG & NEAL J. EVANS II

*Draft version June 19, 2018*

### ABSTRACT

We present an evolutionary picture of a forming star. We assume a singular, isothermal sphere as the initial state of the core that undergoes collapse as described by Shu (1977). We include the evolution of a first hydrostatic core at early times and allow a disk to grow as predicted by Adams & Shu (1986). We use a 1-dimensional radiative transfer code to calculate the spectral energy distribution for the evolving protostar from the beginning of collapse to the point when all envelope material has accreted onto the star+disk system. Then, we calculate various observational signatures ( $T_{bol}$ ,  $L_{bol}/L_{smm}$ , and infrared colors) as a function of time.

As defined by the bolometric temperature criterion, the Class 0 stage should be very short, while the Class I stage persists for much of the protostar's early life. We present physical distinctions among the classes of forming stars and calculate the observational signatures for these classes. Finally, we present models of infrared color-magnitude diagrams, as observed by the Spitzer Space Telescope, that should be strong discriminators in determining the stage of evolution for a protostar.

*Subject headings:* stars: formation, low-mass

### 1. INTRODUCTION

In 1977, Shu presented seminal work in the theory of low-mass, isolated star formation (Shu 1977, hereafter Shu77). He presented the idea that stars could form from inside-out collapse. This model is still important today because it is simple, yet it predicts so many observables in the process of star formation. It prescribes the evolution of inflow, the velocity structure of the envelope, and the particular shape of the envelope's density distribution. Motte & André (2001) found that the inside-out collapse model fit millimeter observations of protostars in Taurus and various Bok globules. However, these authors also found Class 0 sources in Perseus, a less quiescent region of star formation, that had central densities and accretion rates that were too high to be accounted for by the Shu77 model. Molecular line observations have also been used to compare the predicted densities and velocities with the actual conditions in star-forming cores. Hogerheijde & Sandell (2000) and Zhou et al. (1993) presented evidence that the envelopes of some protostars are undergoing inside-out collapse. Others have presented evidence against inside-out collapse. For example, Tafalla et al. (1998) suggested that L1544, a starless core, exhibits infall motions across the entire core. Nonetheless, it is still not clear whether the Shu77 inside-out collapse scenario or its variants can be ruled out.

Therefore, we have calculated the observational signatures of a star, which is forming through inside-out collapse, so that astronomers can test this theory in a well-defined way. The most relevant aspects of the Shu77 inside-out collapse model are a constant accretion rate of material from the envelope onto the star+disk system and an envelope density that is initially described by a singular, isothermal sphere (SIS).

The constant accretion rate in this model has given rise to the so-called "luminosity problem": the luminosities that result when material accretes onto a central object with a small radius and increasing mass exceed those seen

for most young, low-mass stars (Kenyon & Hartmann 1995). The presence of a disk can help by increasing the accretion radius and acting as a reservoir where matter is stored and then episodically accreted. However, a disk does not completely eliminate the "luminosity problem" in these models.

A constant accretion rate in star-forming cores should be evident when comparing populations in the different stages of star formation. The transition from Class 0 to Class I object is thought to occur when the mass of the star and disk is equal to the envelope mass. Therefore, we should observe equal numbers of Class 0 and I objects if they form with constant accretion rates. André & Montmerle (1994) found about a 10:1 ratio for Class I and 0 sources in Ophiuchus, suggesting the Class 0 stage is very short. However, Visser et al. (2002), in an unbiased survey of dark clouds, found a 1:1 ratio. These authors suggested that Ophiuchus has experienced a burst of star formation in the past, resulting in the 10:1 ratio. Future and ongoing surveys of nearby star-forming regions will certainly offer more information regarding the relative populations of Class 0 and Class I sources (Evans et al. 2003; Benjamin et al. 2003).

The initial density configuration for the Shu77 model is that of a SIS, which has  $n(r) \propto r^{-2}$ . One-dimensional modelling of the submillimeter emission from starless cores has shown that their density distributions are well-fitted by Bonnor-Ebert spheres, but power-law density profiles are not conclusively ruled out (Ward-Thompson et al. 1994; Evans et al. 2001). Indeed, some starless cores have a density structure that seems to be approaching the SIS. For example, three-dimensional modelling of L1544 shows a power-law density distribution with  $n(r) \propto r^{-2}$  (Doty et al. 2005). Other studies of the density distribution in more evolved star-forming cores were unable to rule out the Shu77 predictions (Young et al. 2003); in fact, one-third of the sources in Young et al. (2003) were well-fitted by the inside-out collapse model. For this paper, we assume that starless cores must evolve into an SIS. At this point, col-

lapse ensues, and we begin modeling the evolution of the protostar. This work has been expanded by Lee et al. (2004) to model the chemical evolution of these star-forming cores.

Other authors have predicted the observed signatures of a forming star. Myers et al. (1998), hereafter M98, developed a framework on which to calculate various signatures of star formation. Our work has been prompted by their efforts. However, the methods and models employed in this work are quite different from those of M98; as a result, our conclusions are different. We discuss these differences in this paper.

Because these models are 1-dimensional, we do not consider the role of outflows, flattened envelopes, or asymmetric disks; therefore, we probably underestimate the amount of short-wavelength radiation. Whitney et al. (2003, hereafter W03) have included some of these complications. However, W03 did not create a consistent evolutionary model but, instead, considered “typical” protostellar objects of different observational classes. Fortunately, these authors were able to explore the impact of 3-dimensional effects, which we are unable to model. In this way, we consider this effort to be complementary to the work of W03 and compare our results to theirs.

The advent of large surveys such as 2MASS and the Spitzer Space Telescope’s Legacy programs (Evans et al. 2003; Benjamin et al. 2003) provide vast sets of data through which theories of star formation may be vigorously tested. In this work, we hope to provide some tangible means to study the validity of the inside-out collapse model in the role of forming stars.

## 2. THE MODEL

First, we define the framework through which we have created this evolutionary sequence. In this section, we discuss what has been assumed for the dust opacity, interstellar radiation field, envelope structure and dynamics, and the evolution of the star and disk components of the system.

### 2.1. Interstellar Radiation Field & Dust Properties

Evans et al. (2001) showed that, for starless cores, the interstellar radiation field (ISRF) significantly affects both the total observed luminosity and the shape of the observed submillimeter intensity profile; even objects with a luminous, internal source might attribute most of their luminosity to the ISRF (Young et al. 2004a). Evans et al. (2001) scaled the ISRF by a constant, but we have used the opacity of Draine & Lee (1984) dust to attenuate the ISRF with  $A_V = 0.5$  (see Figure 8 in Young et al. (2004b)). This method simulates the effects of low density material in the environs of a star-forming core.

These authors (Evans et al. 2001; Shirley et al. 2002; Young et al. 2003) also found that the multi-wavelength observations were best matched by using the opacities of the dust modeled by Ossenkopf & Henning (1994). In particular, they concluded that “OH5” dust, found in the fifth column of Table 1 in Ossenkopf & Henning (1994), was optimal for star-forming cores. Unfortunately, the modeled data for OH5 dust does not include wavelengths shortward of 1.25  $\mu\text{m}$ . Ossenkopf & Henning (1994) calculated only the values for the dust opac-

ity ( $\kappa$ ) and not the scattering and absorption cross-sections ( $\sigma_{abs}$  and  $\sigma_{scat}$ ) as needed by DUSTY, the radiative transfer program we have used (Ivezic et al. 1999; Ivezic & Elitzur 1997). Therefore, we have obtained data from Pollack et al. (1994), which includes the scattering and absorption cross-sections for wavelengths as short as 0.091  $\mu\text{m}$ . In Figure 1, we show the opacities for OH5 dust and the opacity calculated by Pollack et al. (1994) for dust grains with a radius of 0.1  $\mu\text{m}$  at a temperature of 10 K (hereafter, P1 dust); we have assumed a gas-to-dust ratio of 100 and give the opacity of the gas in this figure. At short wavelengths, these two types of opacities are in fairly good agreement; unless  $\tau$  is low, however, the short-wavelength opacity is not relevant. We used the opacity given for OH5 and  $\sigma_{scat}$  for the P1 dust to calculate the absorption coefficient for the OH5 dust. Further, we used the albedo values given by Pendleton (1990, Figure 4b) to apportion the opacity due to scattering and absorption from the 3  $\mu\text{m}$  ice feature. Finally, we have extrapolated the cross-sections out to 3.6 cm, as required by DUSTY. For  $\sigma_{scat}$ , we extrapolate by a  $\lambda^{-4}$  power-law as expected for Rayleigh scattering. We fit the last several data points of the OH5 absorption coefficients to determine the  $\lambda^{-1.8}$  power-law used to extrapolate  $\sigma_{abs}$  out to  $\lambda = 3.6$  cm. We show the scattering and absorption coefficients in Figure 1.

### 2.2. Envelope

For the density structure in the envelope, we adopt the inside-out collapse scenario (Shu 1977). This model begins with an SIS with a density distribution that is proportional to  $r^{-2}$ . Through some perturbation, collapse begins inside the cloud and proceeds outward. As collapse ensues, the cloud’s density distribution can be approximately described by a broken power law: the inner collapsing portion,  $n \propto r^{-3/2}$  (indicative of freefall), and the outer static envelope,  $n \propto r^{-2}$ . However, there is a transition region just within the infall radius where the density profile is significantly flatter than the  $r^{-3/2}$  power law. Therefore, we use the actual solutions to Equations 11 and 12 in Shu (1977).

When the infall radius exceeds the outer radius, the Shu77 solution is no longer valid. Therefore, we adopt a density profile with  $n \propto r^{-3/2}$  and let the mass of the envelope (and, hence, the fiducial density) decrease as mass is accreted onto the protostar and disk.

The total amount of mass is constrained by the effective sound speed ( $c_s$ ) and the envelope’s outer radius ( $r_o$ ). The models presented herein all begin with cores whose initial masses are different. We calculate this mass from the following expression:

$$M_{env}^{t=0} = \frac{2c_s^2 r_o}{G}, \quad (1)$$

where  $G$  is the gravitational constant, and  $c_s$  is the effective sound speed,

$$c_s = \left( \frac{kT}{\mu m_H} + \frac{1}{2} v_{turb}^2 \right)^{1/2}, \quad (2)$$

where  $k$  is Boltzmann’s constant,  $T$  is the isothermal temperature,  $\mu$  is the mean molecular mass ( $\mu = 2.29$ ), and  $m_H$  is the mass of the hydrogen atom ( $m_H = 1.6733 \times 10^{-24}\text{g}$ ) and  $v_{turb}$  is the turbulent velocity (1/e

Doppler width). We choose  $T = 10$  K and the value for  $v_{turb}$  such that the turbulent contribution to the sound speed is equal to the thermal component ( $v_{turb} = 0.268$  km s $^{-1}$ );  $c_s = 0.268$  km s $^{-1}$ .

We calculate the total envelope mass as follows,

$$M_{env} = \mu m_H \int_{r_i}^{r_o} 4\pi r^2 n(r) dr, \quad (3)$$

where  $r_i$  and  $r_o$  are the inner and outer radii of the envelope. In this paper, radii pertaining to the envelope are denoted by the lower-case “r” ( $r_i$ ,  $r_{inf}$ , and  $r_o$ ) while the radii of the star and disk are denoted by the upper-case “R” ( $R_*$ ,  $R_i$ ,  $R_D$ ).

Even though the Shu77 model has no specific mass scale, we assume that the model is applicable to the formation of stars with different masses. In order to define the mass of the core, we truncate the outer radius of the envelope, using Equation 1. Such truncated envelopes are not unheard of; Motte et al. (1998) found evidence for truncated outer radii for cores in Ophiuchus. In this paper, we consider cores with three initial masses: 0.3, 1.0, and 3.0 M $_{\odot}$ . With our assumed sound speed, these masses correspond to outer radii of 1767, 5889, and 17667 AU. We end our modeling when all envelope material has accreted onto the star-disk system. In these three scenarios, this event occurs at 62500, 210000, and 625000 years, respectively. The time for collapse varies significantly among the three models, but this variation is inherent within the inside-out collapse model, assuming similar initial conditions. With constant and identical accretion rates, lower-mass objects simply form more quickly than higher-mass objects. We show the mass evolution for each of these cases in Figure 2.

It is not clear whether this model is realistic for cores with masses as low as 0.3 M $_{\odot}$ . The Jean’s mass for a core with  $T = 10$  K and density of 10 $^6$  cm $^{-3}$  is  $\sim 0.6$  M $_{\odot}$  ( $M_J = 18M_{\odot}T_K^{1.5}n^{-0.5}$ ). However, if the cloud is cooler, it could be unstable to collapse (e.g., if  $T = 5$  K and  $n = 10^6$ ,  $M_J = 0.2$  M $_{\odot}$ ). In fact, much smaller mass cores can be created through turbulent fragmentation (Boyd & Whitworth 2005), so the 0.3 M $_{\odot}$  is probably not so absurd. Considering that some evolved protostars are thought to be substellar (White & Hillenbrand 2004), we must consider how these objects are formed.

Defining the envelope’s inner radius is an issue. One choice is that the envelope’s inner radius could be equal to the outer radius of the disk. However, this disk radius, which is defined as the centrifugal radius (Section 2.3.1), is very small at early times. With a small inner radius, the density in the inner region is unrealistically large (e.g.,  $n \sim 10^{10}$  cm $^{-3}$ ). These dense regions cause the opacity to become very high. Further, a rotating envelope becomes flattened and aspherical at these small radii (Terebey et al. 1984), so a spherical model is not appropriate to these regions. Therefore, we set a maximum value for  $\tau(100 \mu\text{m})$  and calculate the inner radius of the SIS (at  $t = 0$ ) so that  $\tau_{\nu}(100\mu\text{m})$  is equal to  $\tau_{max}$ .

$$r_i = \left[ \frac{\tau_{max} G 2\pi}{\kappa_{\nu} c_s^2} + \frac{1}{r_o} \right]^{-1} \quad (4)$$

We choose  $\tau_{max} = 10$  and discuss the impact of varying this in section 6.3. The envelope’s inner radius follows

this formula until it is exceeded by the disk radius. For the three cores, the envelope’s inner radius is 100 AU at the end of collapse (see Section 2.3.1).

We define the infall rate for the case of a non-magnetic, centrally peaked envelope density distribution as described in the Shu (1977) scenario. The rate of constant accretion is calculated as follows:

$$\dot{M} = m_o \frac{c_s^3}{G}, \quad (5)$$

where  $m_o$  is a dimensionless constant of order unity. Since  $c_s = 0.268$  km s $^{-1}$ , the accretion rate,  $\dot{M}$ , is  $4.8 \times 10^{-6}$  M $_{\odot}$  yr $^{-1}$ .

We adopt the prescription of Adams & Shu (1986) for the infall rate onto the disk and star. These authors assume that all mass is accreted onto either the disk or star such that  $M = M_* + M_D$  where  $M_*$  is the accretion rate of envelope material directly onto the star and  $M_D$  is the accretion rate onto the disk. These values are calculated as follows:

$$\dot{M}_* = \dot{M}[1 - (1 - u_*)^{1/2}], \quad (6)$$

$$\dot{M}_D = \dot{M}(1 - u_*)^{1/2}, \quad (7)$$

where  $u_*$  is the ratio of the star and disk radii,  $R_*/R_D$ . In almost all cases,  $u_*$  becomes very small in a short time and, hence,  $\dot{M}_*$  also approaches zero. However, material also accretes from the disk onto the star; this process is not included in these equations. Adams & Shu (1986) defined an efficiency factor— $\eta_D$ , the fraction of material in the disk that will accrete onto the star—so that the star could gain mass and be a source of accretion luminosity. We discuss the implementation of this accretion process in the next section.

### 2.3. Disk

Evidence in the form of near- and mid-infrared (Padgett et al. 1999) and millimeter (Mundy et al. 1996; Kitamura et al. 2002) observations of disks surrounding stellar and substellar objects has recently become more convincing. Also, the inclusion of a disk in various models has a significant effect on the interpretations of those models. Therefore, to not include a disk in this evolutionary scheme is wholly unrealistic.

We adopt the disk model developed, in theory, by Adams, Shu, & Lada (1988), and, in practice, by Butner et al. (1994). The density distribution for the dust and gas (assuming homogeneous mixing) is defined as

$$\Sigma(R) = \Sigma_o \left( \frac{R}{R_f} \right)^{-p}, \quad (8)$$

where  $\Sigma_o$  is the surface density (in gm/cm $^2$ ) at  $R_f$ , a fiducial radius. We choose  $p = 1.5$  in accordance with the density structure for vertical hydrostatic equilibrium (Chiang & Goldreich 1997). The mass of the disk, given this power law distribution is given by:

$$M_D = \int_{R_i}^{R_D} 2\pi \Sigma R dR = \frac{2\pi \Sigma_o R_f^p}{2-p} (R_D^{2-p} - R_i^{2-p}), p < 2, \quad (9)$$

where  $R_i$ ,  $R_D$ , and  $R_f$  are the inner, outer, and fiducial radii of the disk.

### 2.3.1. Radius of the Disk

The inner radius of the disk is the dust destruction radius defined as:

$$R_i = \sqrt{\frac{L_*}{4\pi\sigma T_{dust}^4}}, \quad (10)$$

where we define the dust destruction temperature,  $T_{dust} = 2000$  K, and  $L_*$  is the luminosity of the star.

For the disk outer radius,  $R_D$ , we adopt the centrifugal radius that evolves with time as follows (Terebey et al. 1984),

$$R_D(t) = \frac{m_\odot^3}{16} c_s t^3 \Omega_\odot^2, \quad (11)$$

where  $t$  is the time and  $\Omega_\odot$  is the angular velocity of the cloud prior to collapse; other variables are as already defined. We set  $\Omega_\odot$  so that, at the end of the Class I stage, the disk radius is 100 AU. These angular velocities are  $1 \times 10^{-14}$ ,  $5.5 \times 10^{-14}$ , and  $3.4 \times 10^{-13}$  s $^{-1}$  for the 3, 1, and  $0.3 M_\odot$  models, respectively. Goodman et al. (1993) found a range for  $\Omega_\odot$  from  $9.7 \times 10^{-15}$  to  $1.3 \times 10^{-13}$  s $^{-1}$ . The upper end of this range is about one-third of  $\Omega_\odot$  for the  $0.3 M_\odot$  model, but the least massive of the cores in Goodman et al. (1993) was  $0.6 M_\odot$ . We assume that less massive and smaller cores have higher angular velocities.

### 2.3.2. Mass of the Disk

We evolve the mass of the disk via the expression given by Adams & Shu (1986):

$$M_D = (1 - \eta_D) \int_{t_o}^t \dot{M}_D dt = (1 - \eta_D) \mathcal{M}_D M, \quad (12)$$

where  $t_o$  is the time when  $u_* = 1$  (i.e.,  $R_D = R_*$ ). We assume  $t_o = 0$ . Further, Adams & Shu (1986) defines  $\mathcal{M}_D$  as follows:

$$\mathcal{M}_D = \frac{1}{3} u_* \int_{u_*}^1 (1 - u_*)^{1/2} u^{-4/3} du. \quad (13)$$

We evaluate this expression numerically as suggested by Adams & Shu (1986). Finally,  $M$  is the total mass accreted (i.e.  $M = \dot{M}t$ ). Adams & Shu (1986) give  $\eta_D$  as a free parameter;  $\eta_D$  is the fraction of material accreted onto the disk that will eventually accrete onto the star. To determine a value for  $\eta_D$ , we assume that the ratio of star to disk mass must be  $\sim 1/4$ , which is in accord with theoretical work (Li 2002). In Figure 3, we show this ratio for several values of  $\eta_D$ . We choose  $\eta_D = 0.75$  so that  $M_D/M_* \sim 1/4$  for the  $1 M_\odot$  model. We apply the same criterion for the  $0.3$  and  $3 M_\odot$  models and set  $\eta_D = 0.7$  and  $\eta_D = 0.9$ , respectively. In section 6, we explore the effects of allowing it to vary.

### 2.3.3. Luminosity of the Disk

The temperature distribution for the disk is defined by the following,

$$T(R) = T_\odot \left( \frac{R}{R_f} \right)^{-q} (K), \quad (14)$$

where  $T_\odot$  is the temperature at the fiducial radius,  $R_f$ . We set  $q = 0.5$ , a temperature distribution that decreases more slowly with radius than expected for a flat disk, to

simulate flaring and disk accretion (Butner et al. 1994; Kenyon & Hartmann 1987).

The luminosity of the disk has several components as given by Adams & Shu (1986). First, envelope material falling onto the disk will act as a source of luminosity. Then, there is a source of “mixing luminosity” that arises, basically, from the mixing of newly accreted material and that material already in orbit around the star. Finally, Adams & Shu (1986) assumed that some fraction ( $\eta_D$ ) of the disk material will frictionally dissipate its remaining orbital energy and fall onto the star. Adams & Shu (1986) give the expression for  $L_{acc}^D$  in equation 33b of their work; we use this equation for  $L_{acc}^D$ , which includes all three of these components, in the evolutionary model. As the disk radius grows larger with time and  $u_* \rightarrow 0$ , their expression for  $L_{acc}^D$  simplifies to (Adams, Lada & Shu 1987)

$$L_{acc}^D \approx \frac{1}{2} \eta_D L_\odot, \quad (15)$$

$$\text{where } L_\odot \equiv \frac{GM_*\dot{M}_*}{R_*}.$$

## 2.4. Star

For the star, we define several parameters: mass ( $M_*$ ), luminosity ( $L_*$ ), radius ( $R_*$ ), and effective temperature ( $T_{eff}$ ). Each of these quantities evolve over time, and they are generally interdependent.

### 2.4.1. Mass of the Star

For the stellar mass, we subtract the disk mass from the total accreted mass as in Adams & Shu (1986):

$$M_* = M - M_D = [1 - (1 - \eta_D) \mathcal{M}_D] M. \quad (16)$$

All variables are as previously defined. Included in this equation are two means by which the star gains mass. Material accretes directly from the envelope onto the star until the disk grows in size and accretes most of the infalling envelope mass. Then, the star mostly gains material that has accreted onto and is processed through the disk.

### 2.4.2. Luminosity of the Star

The luminosity of the star has two components: that arising from accretion ( $L_{acc}^*$ ), the dominant source of luminosity at early times, and the luminosity due to gravitational contraction and deuterium burning ( $L_{phot}$ ). Simply,  $L_* = L_{acc}^* + L_{phot}$ .

Adams & Shu (1986) calculate the accretion luminosity from material accreting onto the star. Their calculations include the luminosity from material that falls onto the star and the energy released due to differential rotation of the protostar. Adams & Shu (1986) give an expression for  $L_{acc}^*$  in equation 33a of their work; we use this prescription for  $L_{acc}^*$ . As the disk radius grows larger with time and  $u_* \rightarrow 0$ , this simplifies to (Adams, Lada & Shu 1987)

$$L_{acc}^* \approx \frac{1}{2} \eta_D^2 \eta_* L_\odot. \quad (17)$$

Adams & Shu (1986) define  $\eta_*$  as an “efficiency factor” that dictates how the star dissipates the energy due to differential rotation. Adams, Lada & Shu (1987) considered this value to be a free parameter but chose  $\eta_* = 0.5$

for their standard model, which we use as well. In section 6, we discuss the effects of varying  $\eta_*$ .

$L_{phot}$  was calculated by D'Antona & Mazzitelli (1994, hereafter DM). We have made linear fits to their pre-main sequence tracks with opacities from Alexander et al. (1989) (Tables 1 and 5 of DM). First, we have fit a power-law in the luminosity-time plane for each stellar mass given by DM. For masses less than  $0.2 M_\odot$ , where a single power-law is not appropriate, we have fit two-piece power-laws to DM's data. For times earlier than those covered by DM's tracks, we have assumed a power-law expression:  $L_{phot} = L_\odot^{phot} \left( \frac{t}{t_\odot} \right)^5$ , where  $t_\odot$  is the earliest time in the calculations by DM, and  $L_\odot^{phot}$  is the luminosity of the pre-main sequence star at time  $t_\odot$ . This equation is ad hoc and meant to smoothly bridge the transition from where there is no data for  $L_{phot}$  to the point where DM's evolutionary tracks begin. Finally, to obtain the appropriate value for  $L_{phot}$ , we linearly interpolate between masses for a given time in the star's evolution.

As noted in M98, the beginning of infall and accretion luminosity is not the same time as that for the onset of the luminosity represented by  $L_{phot}$ . We adopt, as M98 did, a difference in these two timescales of  $10^5$  years such that, for  $L_{phot}(t)$ , we take  $t = t_{phot} + 10^5$  yr for particular values of  $t_{phot}$  as given by DM; this assumption is based on the theoretical work of Stahler (1983). After collapse begins, the forming star must wait  $10^5$  years before the luminosity due to contraction and deuterium burning (as described by DM) will begin. Further, the luminosity from DM's models does not become significant until  $\sim 7 \times 10^4$  years. Therefore,  $L_{phot}$  is not relevant until  $t \sim 1.7 \times 10^5$  years, which is greater than the time required for the  $0.3 M_\odot$  to collapse and only  $4 \times 10^4$  years more than the collapse time for the  $1 M_\odot$  core.

With this final term, the total luminosity of the protostellar system is now made of three components:  $L_{acc}^*$ , the luminosity due to accretion and differential rotation of the protostar;  $L_{phot}$ , the luminosity arising from gravitational contraction and deuterium burning in the protostar, and  $L_{acc}^D$ , the luminosity from accretion onto the disk and dissipation of the orbital energy within the disk.

In addition, there is the luminosity that results from the ISRF,  $L_{ISRF}$ . We calculated  $L_{ISRF}$  by illuminating a core that has no internal source. However, the core does have an evolving density distribution identical to the three mass scenarios presented herein. Then, we calculate the luminosity that results from the dust grains, which are heated externally. At early times, the external radiation field contributes most of the luminosity. As the envelope mass decreases and the internal source luminosity grows,  $L_{ISRF}$  becomes insignificant. We plot the evolution of  $L_{ISRF}$  in Figure 4.

In conclusion, the total luminosity is given as

$$L_{tot} = L_{acc}^* + L_{phot} + L_{acc}^D + L_{ISRF}. \quad (18)$$

For  $T_{eff}$ , we use the Stefan-Boltzmann Law,

$$T_{eff} = \left( \frac{L_*}{\sigma 4\pi R_*^2} \right)^{1/4}, \quad (19)$$

where  $L_* = L_{acc}^* + L_{phot}$ . At early times, the effective temperature is very low,  $\sim 100$  K because the radius of

the first hydrostatic core (Section 2.4.3) is  $\sim 5$  AU. When the stellar radius approaches  $2-5 R_\odot$ ,  $T_{eff}$  becomes more stellar-like ( $\sim 3000$  K).

#### 2.4.3. Radius of the Star - Simulating the FHC

We allow the radius of the star to evolve as suggested by Palla & Stahler (1991, see Figure 1 in their paper). In their calculations, they find that the radius of the star rises to about 2-5 solar radii; this result is in accord with the assumption of a constant radius at  $3 R_\odot$  by M98. However, the time at which to apply these calculations is not so clear.

In the evolution of a protostar, the early years are occupied by the first hydrostatic core. While not yet clearly observed, the first hydrostatic core has been predicted (Boss & Yorke 1995; Masunaga et al. 1998). Boss & Yorke (1995) concluded, based on some simple arguments, that the lifetime of this stage should be short, only about 20,000 years. Further, Masunaga et al. (1998) have determined that the average radius of this core should be about 5 AU. The transition between this very large core and the smaller core described by the calculations of (Palla & Stahler 1991) is not well-understood. We have assumed the stellar radius evolves as shown in Figure 5. In the beginning, the radius of the first hydrostatic core is 5 AU. At  $t=20,000$  years, we allow the radius to decrease from 5 AU to the radius calculated by Palla & Stahler (1991). This transition lasts 100 years and is described, in our model, by:

$$R_*(AU) = 5 \left[ 1 - \left( \frac{t - 20000}{100} \right)^{0.5} \right] + R_*^{PS}, \quad (20)$$

$20,000 < t < 20,100$

where  $t$  is the time in years and  $R_*^{PS}$  is the value for the radius calculated by Palla & Stahler (1991). This equation is somewhat ad hoc and simply used to simulate the transition between the large radius as predicted by Masunaga et al. (1998) and the much smaller radius of the actual star as predicted by Palla & Stahler (1991).

There are consequences for including this large radius at early times. Because the centrifugal radius is very small and, hence, the disk has not formed, the luminosity at these early times is derived wholly from spherical accretion onto the central source. If this central source is small, the accretion luminosity can be very high. In Figure 6, we show the evolution of the accretion luminosity for two scenarios. In one case, we have included the FHC. We also plot  $L_{acc}^*$  when there is no FHC. In this case, the stellar radius evolves via the data of Palla & Stahler (1991) (i.e., between 2 and  $5 R_\odot$ ). Without a FHC, the accretion luminosity rises quickly because there is no disk and material is accreting directly onto the star. At about  $2 \times 10^4$  years, the centrifugal radius has increased so that a disk can form. Then, the accreting material is processed by the disk causing  $L_{acc}^*$ , which arises from accretion onto the star, to decrease.

In summary, we let the mass of the star and the accretion luminosity evolve as defined by Adams & Shu (1986), the radius of the star change as predicted by Palla & Stahler (1991) (except at early times), and the luminosity due to deuterium burning and gravitational contraction of the PMS star evolve as calculated by DM.

The effective temperature, given these other factors, is defined by the Stefan-Boltzmann Law.

### 3. SIGNATURES

In this section, we discuss the various observational signatures in the evolution of protostellar systems.

We calculate the bolometric temperature by the prescription given in Myers & Ladd (1993),

$$T_{bol} \equiv [\zeta(4)/4\zeta(5)]h\bar{\nu}/k = 1.25 \times 10^{-11}\bar{\nu}, \quad (21)$$

where  $\zeta(m)$  is the Riemann zeta function of argument  $m$ ,  $h$  is Planck's constant,  $k$  is Boltzmann's constant, and the mean frequency,  $\bar{\nu}$ , is the ratio of the first and zeroth frequency moments:

$$\bar{\nu} \equiv I_1/I_0, I_m = \int_0^{\infty} \nu^m S_{\nu} d\nu. \quad (22)$$

In addition, we calculate the bolometric luminosity:

$$L_{bol} = \int_0^{\infty} 4\pi D^2 S_{\nu} d\nu \quad (23)$$

where  $S_{\nu}$  is the flux density, and  $D$  is the distance. We set  $D = 140$  pc, suitable for nearby star-forming regions. We also calculate  $L_{bol}/L_{smm}$  for our models (André et al. 1993).  $L_{smm}$  is found by integrating Equation 23 from  $350 \mu\text{m}$  to  $\infty$ .

We also calculate the fluxes that would be seen by the photometric bands on the Spitzer Space Telescope by convolving the modeled spectral energy distribution (SED) with the bandpasses for the MIPS instruments. These fluxes do not vary substantially from the monochromatic fluxes for the central wavelength of each bandpass. To convert the fluxes to magnitudes, we use these zero-point fluxes for MIPS bands 1-3 (24, 70, and  $160 \mu\text{m}$ ), respectively: 7.2, 0.8, and 0.17 Jy (Young et al. 2005). We do not convolve the MIPS resolution element with the model but assume that all emission is included within this beam.

### 4. RADIATIVE TRANSFER

We use the radiative transfer code, DUSTY, as developed by Ivezić et al. (1999) to calculate the temperature distribution in the envelope and the emergent SED of the star, disk and envelope. In this section, we discuss the effect and treatment of scattering by dust grains in these calculations.

DUSTY assumes that scattering from dust grains is isotropic. Longward of  $10 \mu\text{m}$ , the SED is barely affected because the scattering cross-section ( $\sigma_{scat}$ ) is significantly less than the absorption cross-section ( $\sigma_{abs}$ , see Figure 1). Further, the effect is also minimal at wavelengths shortward of  $10 \mu\text{m}$  when the interstellar radiation field is not included.

Unfortunately, the assumption of isotropic scattering causes some problems when the interstellar radiation field is included. In Figure 7, we show the SED for a core with a mass of  $1 M_{\odot}$  (with  $\tau_{100\mu\text{m}} = 1$ ). In these models, the only heating of the dust grains is externally from the ISRF. For the solid line, we include the effects of isotropic scattering by the dust grains while the dashed line shows the SED without scattering. Both SEDs have a peak

at submillimeter wavelengths as is expected. However, the SED with scattering included also has a peak in the near-infrared. Of course, we do not observe strong near-infrared radiation from starless cores. At short wavelengths, these dust grains preferentially forward scatter light, so neglecting the anisotropic nature of the scattering causes this unrealistic flux in the near-infrared.

Our options are either a) neglect the effects of scattering in calculating the emergent SED or b) ignore the ISRF. The latter is not really feasible because, at early times, the ISRF provides the sole source of heating and, hence, ignoring it radically affects the temperature profile for the core. Therefore, we opt for the first alternative and ignore the effects of scattering.

### 5. AN EVOLVING PROTOSTAR

With these methods and assumptions, we have calculated the SED for an evolving protostar. In Figure 8, we show the SED for particular times in the evolution of the core that began with a pre-collapse mass of  $1 M_{\odot}$ . We have also set  $\tau_{max} = 10$ ,  $\eta_D = 0.75$ , and  $\eta_* = 0.5$  (see sections 2.2, 2.3.2, and 2.4.2). The solid line is the emergent SED as observed at 140 pc, the distance to Taurus. The dashed line represents the star+disk SED; this spectrum is for the central source and is the input for DUSTY. The bars represent the sensitivity for the Spitzer Space Telescope c2d Legacy program (Evans et al. 2003); we have increased the  $70 \mu\text{m}$  sensitivity by a factor of three based on in-flight performance. The asterisks in the second frame are IRAS sensitivities.

We calculate the observational signatures, described in Section 3, for models with different initial conditions and whose evolution proceeds in different ways. We use different timesteps for the models:  $\Delta t = 1000, 2000$ , and  $6000$  years for the  $0.3, 1$ , and  $3 M_{\odot}$  models, respectively. These timesteps are each about 1% of the total infall time.

### 6. FREE PARAMETERS

In this section, we explore the effects of various parameters in these models. We show how the model changes when we use different values for  $\eta_D$ ,  $\eta_*$ , and  $\tau_{max}$ . We find that neither  $\eta_D$  or  $\eta_*$  have a large effect on the observational signatures of the SEDs, but the choice for  $\tau_{max}$  can significantly affect the short-wavelength emission during all stages of evolution. We adopt these values:  $\eta_D = 0.75$ ,  $\eta_* = 0.5$ , and  $\tau_{max} = 10$ .

#### 6.1. $\eta_D$

This factor determines what fraction of the disk material will dissipate its energy and accrete onto the star. It is relevant in the calculation of the disk mass ( $M_D$ , equation 12), the disk accretion luminosity ( $L_{acc}^D$ , equation 15), the mass of the star ( $M_*$ , equation 16), and the stellar accretion luminosity ( $L_{acc}^*$ , equation 17).

We show the effects of changing  $\eta_D$  for the  $1 M_{\odot}$  core in Figure 9. Varying  $\eta_D$  alters the evolution of all components of the luminosity. Of course, this parameter is included directly in the equations for the disk and stellar accretion luminosities. Because  $\eta_D$  determines the stellar mass, it also affects the luminosity due to deuterium burning and contraction ( $L_{phot}$ ). With  $\eta_D = 0.75$ , each of these are higher than in the other two scenarios ( $\eta_D = 0.25$  &  $0.5$ ).

Finally, in the left panels of Figure 10, we show how changing  $\eta_D$  affects observational signatures. We plot  $T_{bol}$  and  $L_{bol}/L_{smm}$  versus time with  $\eta_D = 0.25, 0.5$ , and  $0.75$ . Variations in  $\eta_D$  have almost no effect on the evolution of  $T_{bol}$ , and  $L_{bol}/L_{smm}$  only varies slightly for the different values of  $\eta_D$ .

### 6.2. $\eta_*$

This factor is a measure of how much of the total luminosity arises from the central star. In practice, it is only relevant for the accretion luminosity,  $L_{acc}^*$ , as in equation 17. In Figure 11, we plot the evolution of  $L_{acc}^*$  for different values of  $\eta_*$ . The value that we choose for this “efficiency factor” does considerably change the accretion luminosity. However, as shown by Figure 10, the value for  $\eta_*$  has very little effect on the observational signatures. For the standard model in this paper, we adopt  $\eta_* = 0.5$ .

### 6.3. $\tau_{max}$

As discussed in section 2.2, the inner radius of the envelope is set so that  $\tau(100\mu\text{m})$  does not exceed a certain value. Previously, some have proposed that the condition of isothermality is violated if  $\tau(100\mu\text{m}) > 1$  (Larson 1969). However, Masunaga & Inutsuka (1999) showed that  $\tau(100\mu\text{m})$  could be significantly greater than 1 while the core still maintains isothermality.

In Figure 12, we plot the evolution of  $\tau_\nu(100\mu\text{m})$  with  $\tau_{max} = 1, 5, 10$ , and  $15$ . The density profile begins with a distribution of  $n(r) \propto r^{-2}$ , but, as collapse begins, the inner region drops to a considerably shallower profile. Because the inner density profile changes,  $\tau$  drops considerably. In Figure 13, we show the SED of a  $1 M_\odot$  core at  $t = 4 \times 10^4$  and  $10^5$  years with  $\tau_{max} = 1, 10$ , and  $15$ . The model with  $\tau_{max} = 1$  shows more emission at shorter wavelengths than those with higher  $\tau_{max}$ . The SED with  $\tau_{max} = 10$  is almost identical, at all times, to that with  $\tau_{max} = 15$ .

In Figure 12, there is a discontinuity at  $\sim 1 \times 10^5$  years. This is the point where the infall radius exceeds the outer radius of the infalling envelope. At this point, we changed from the Shu (1977) solution to an envelope whose density is described by  $n(r) \propto r^{-3/2}$ . This is not a perfect transition, however, so the “kink” at  $\sim 1 \times 10^5$  years is an artifact of the model.

We explore the effects of changing  $\tau_{max}$  on the observational signatures of our evolving protostar. In Figure 14, we show the evolution of  $T_{bol}$  and  $L_{bol}/L_{smm}$  for the different values of  $\tau_{max}$ . The bolometric temperature is most affected by varying  $\tau_{max}$ ; higher values for  $\tau_{max}$  slow the transition from a Class I to a Class II protostar (as defined by  $T_{bol}$ ). Simply, less short-wavelength radiation can escape the cloud when the opacity is higher. However, for those models with  $\tau_{max} \geq 5$ , the evolution of  $T_{bol}$  begins to converge. Finally, not surprisingly,  $L_{bol}/L_{smm}$  is unaffected by changing  $\tau_{max}$ . We do not significantly alter the mass of the envelope, which dictates  $L_{smm}$ , nor the accretion processes, which are responsible for  $L_{bol}$ .

The actual value for  $\tau_{max}$  is highly uncertain. We do not fully understand the density structure in this transition area between the envelope and disk nor do we include the geometrical effects of a flattened envelope in

this region. We assume that  $\tau_{max} = 10$ ; higher values of  $\tau_{max}$  have little effect on observed quantities (i.e., the SED and its derived signatures). The peak of a  $10\text{ K}$  blackbody is  $350\mu\text{m}$ . Assuming  $\kappa \propto \lambda^{-1.5}$ ,  $\tau_{350\mu\text{m}} = 1.5$  when  $\tau_{100\mu\text{m}} = 10$ .

## 7. RESULTS

With these free parameters set to the given values, we have run models with different initial masses:  $0.3, 1.0$ , and  $3.0 M_\odot$ . Then, we have calculated the various observational signatures.

### 7.1. $T_{bol}$ and $L_{bol}/L_{smm}$

The bolometric temperature and the ratio of bolometric to submillimeter luminosity have emerged, in the past decade, as the two primary methods of classifying protostars. Because  $T_{bol}$  is a measure of the flux-weighted mean frequency of the protostar’s SED, it is highly affected by the emergence of any short-wavelength radiation. The ratio of the bolometric to submillimeter luminosity, on the other hand, is virtually unaffected by the short-wavelength emission. Therefore,  $L_{bol}/L_{smm}$  is less susceptible to the effects of geometry, which can cause more or less NIR radiation to be observed. This ratio is a rough measure of the ratio of protostellar mass (including the disk and star) to the envelope mass.

In Figure 15, we plot the two signatures as they change for the evolving protostar. For the  $0.3 M_\odot$  core, each of the evolutionary indicators increase drastically at about  $2.0 \times 10^4$  years, when the FHC contracts. All of the envelope material has accreted onto the star and disk by  $6.3 \times 10^4$  years, shortly after the central star has contracted from the FHC stage. Therefore, as the central star becomes hotter and more luminous, there is little material left in the envelope. Then,  $T_{bol}$  increases because more short-wavelength radiation is observed, and  $L_{bol}/L_{smm}$  increases because  $L_{smm} \rightarrow 0$  as the envelope goes away. If this model is correct, these low-mass stars should proceed through the FHC stage and, almost immediately, be seen as Class II objects.

The  $1.0$  and  $3.0 M_\odot$  objects track one another fairly well, up to  $10^5$  years, in the  $T_{bol}$  plot (Figure 15) despite the fact that they form on different timescales. The  $1.0 M_\odot$  core requires  $2.1 \times 10^5$  years for all envelope mass to accrete while the  $3.0 M_\odot$  core requires  $6.24 \times 10^5$  years. However, both cores evolve from Class 0 to Class I at about 50,000 years, which is about  $1/4$  and  $1/10$  of the total infall time for the  $1.0$  and  $3.0 M_\odot$  cores, respectively.

This transition from Class 0 to I is partly due to the sudden “turning on” of the central source as it contracts to  $\sim 3 R_\odot$ , and accretion luminosity becomes relevant. There is, however, another reason for this sudden transition. As shown in Figure 12, the Shu77 model exhibits a drastic decrease in  $\tau$  regardless of the adopted value for  $\tau_{max}$ . Initially, the envelope is described by  $n(r) \propto r^{-2}$ , but, as collapse ensues, it changes to  $r^{-3/2}$  and  $\tau$  drops. Because  $\tau$  is so low, any substantial source of stellar luminosity will cause observable short-wavelength radiation to emerge from the system.

These details are actually quite important if one uses these evolutionary signatures to derive relative lifetimes of the various classes as has been done in the past. If one calculates the bolometric temperature for a group of

protostars (whose SEDs have been well sampled), there should be very few Class 0 cores—conservatively, about 1/10 to 1/4 of the Class I population, but most likely a much smaller fraction. Visser et al. (2002) presented their efforts to do such a study; they found approximately equal numbers of Class 0 and I objects. However, their data only included the far-infrared (IRAS) and submillimeter fluxes. Analysis of the mid- and near-infrared data from the Spitzer Legacy and 2MASS surveys along with far-infrared and millimeter observations will almost certainly produce different results. With more complete sampling of the protostars' SEDs, very few Class 0 cores, by the  $T_{bol}$  criterion, should remain if this picture of evolution is correct.

Finally, in the plot of  $T_{bol}$ , the 0.3, 1.0, and 3.0  $M_{\odot}$  data exhibit a “kink” at about  $3 \times 10^4$ ,  $10^5$ , and  $3 \times 10^5$  years, respectively. This is the point where the envelope's density distribution is described by a power-law,  $n(r) \propto r^{-3/2}$ , instead of the Shu77 solution. The power-law distribution has a slightly higher  $\tau$  that causes less short-wavelength radiation to be observed. As a result,  $T_{bol}$  decreases slightly at this point of transition, but this is an artifact of the model.

The ratio of bolometric to submillimeter luminosity seems to be much more consistent in describing the evolution of these protostars. Adopting  $L_{bol}/L_{smm} = 200$  as the dividing line for Class 0 and I cores, we find that the 1 and 3  $M_{\odot}$  protostars become Class I objects after  $1.18 \times 10^5$  and  $3.6 \times 10^5$  years, respectively. These times correspond to slightly more than 1/2 of the total infall time for each core whereas the  $T_{bol}$  criterion showed that the cores became Class I after 1/4 and 1/10 of their total infall times.

Finally, in Figure 16, we show a plot of  $T_{bol}$  and  $L_{bol}/L_{smm}$  for the three models. The points represent data from Young et al. (2003), Shirley et al. (2000), and Froebrich (2005). In general, these models are consistent with the data. However, the 11 starless cores in the lower left-hand section of this plot show higher  $L_{bol}/L_{smm}$  than the model predicts. The definition of  $L_{bol}/L_{smm}$  includes data longward of 350  $\mu\text{m}$ , but, for all of these cores, no 350  $\mu\text{m}$  data exist. Therefore, the observed  $L_{smm}$  is lower than that which is modeled. Second, there is little near- or mid-infrared data available for many of the sources represented. With future observations, the bolometric temperature will almost certainly increase. For example, we consider the 1  $M_{\odot}$  model and calculate  $T_{bol}$  by including different fluxes. If we use IRAS fluxes only,  $T_{bol} = 83$  K for the core at  $5 \times 10^4$  years while  $T_{bol}$ , calculated with just the Spitzer bands, is 92 K. At  $t = 10^5$  years,  $T_{bol}$  is 88 and 151 K as measured with the IRAS and Spitzer fluxes, respectively.

## 7.2. Mass Ratio

We can look at classification from a different, more physical, perspective. In Figure 17, we plot the ratio of the stellar and disk mass to the envelope mass. Physically, we might consider a protostar to move from Class 0 to Class I when this ratio is 1 and there are equal amounts of mass in the protostellar system and the envelope surrounding this star+disk. This event occurs at  $t = 3.1 \times 10^4$ ,  $1.05 \times 10^5$ , and  $3.1 \times 10^5$  years for the 0.3, 1.0, and 3.0  $M_{\odot}$  cores. Of course, as defined by Shu77, this is also the time when the infall radius is equal to the

outer radius.

In Figure 18, we plot  $T_{bol}$  and  $L_{bol}/L_{smm}$  as a function of  $(M_* + M_D)/M_{env}$ . In the  $T_{bol}$  plot, the 1 and 3  $M_{\odot}$  cores change from Class 0 to Class I while  $(M_* + M_D)/M_{env} < 0.5$ . With the presently defined boundaries, the bolometric temperature does not appropriately classify the stages of star formation. Only the 0.3  $M_{\odot}$  core changes from Class 0 to I when  $(M_* + M_D)/M_{env} \sim 1$  as is appropriate for our understanding of these stages.

However, with the  $L_{bol}/L_{smm}$  criterion, we find that the cross-over from Class 0 to I occurs approximately when  $(M_* + M_D)/M_{env} = 1$ , which is a more realistic view of these evolutionary stages. Indeed, this observational signature is also favored because it is not largely dependent on what is observed at short wavelengths where geometric effects play a big role (André et al. 1993).

Therefore, we set some physical divisions for the evolutionary transitions. First, we let the PPC/Class 0 transition occur when the FHC first collapses at  $\sim 2.0 \times 10^4$  years. For all three cores, this occurs when  $L_{bol}/L_{smm} \sim 35$ . For the Class 0/I transition, we let  $(M_* + M_D)/M_{env} = 1$ ;  $L_{bol}/L_{smm} \sim 175$  when this criterion is met. Notice that this value is slightly less than the requirement given by André et al. (1993), i.e.  $L_{bol}/L_{smm} = 200$ . The Class II stage begins when all of the envelope material has been accreted. Our models are not reliable at these late times, and the  $L_{bol}/L_{smm}$  signature is not a very good indicator for this stage of evolution. Nonetheless, we find that  $L_{bol}/L_{smm}$  is approximately 2000 at this point, but this value is dependent on the adopted model for the disk.

## 7.3. BLT Diagrams: A Comparison with M98

In Figure 19, we show a plot of the bolometric luminosity and temperature, which M98 called a BLT diagram. The axes are laid out to mimic the Hertzsprung-Russell diagram with  $T_{bol}$  increasing right to left. In Figure 19, we have included M98's models from Figure 7 in their paper. Two of the thin lines in Figure 19 are their models for forming, 0.5  $M_{\odot}$  protostars whose initial envelope masses were 1 and 3  $M_{\odot}$ . We also show their 0.3  $M_{\odot}$  model from Figure 9, but we label it here as 1.8  $M_{\odot}$  because this is the mass of the envelope before collapse begins while 0.3  $M_{\odot}$  is the mass of the star at  $t=\infty$ . We also plot data from Young et al. (2003), Shirley et al. (2002), and Shirley et al. (2004) as crosses; the dots represent data from Chen et al. (1995) and Chen et al. (1997). Our tracks are markedly different from any of those presented in M98, so a summary of the differences between two models is relevant here. Primarily, our methods differ in that M98 attempts to create a reasonable model that fits the data while we are simply determining the observational signatures of the Shu77 model.

The most significant difference between this work and that of M98 is the assumptions for infall evolution. M98 described the infall and accretion with an exponential decay function such that the accretion rates began at about  $10^{-6} M_{\odot} \text{ yr}^{-1}$  and, as the star approached the main sequence, finished with  $10^{-9} M_{\odot} \text{ yr}^{-1}$ . We assume constant accretion onto the star+disk system throughout the duration of the life of the envelope as predicted by the Shu77 collapse solution. However, in our model, the rate of accretion onto the star's surface does decrease

with time as the disk forms and takes a more prominent role in processing material from the envelope to the star. Also, the modeled evolution is longer for M98 ( $10^6$  years) than in our model ( $2 - 6 \times 10^5$  years).

These different assumptions about infall have several implications. First, in our model, we form a more massive star from similar initial conditions in less time. For our  $3 M_{\odot}$  core, the star reaches  $0.5 M_{\odot}$  at  $t = 132,000$  years. On the other hand, M98's models require, by design, about  $10^6$  years to create this  $0.5 M_{\odot}$  star from a  $3 M_{\odot}$  core. Of course, at the end of  $10^6$  years, the star created by M98 has completed its pre-main-sequence evolution, while our model still requires time to completely accrete the disk material.

This discrepancy in the star's final mass presents another difference between this work and that of M98. M98 included a dispersal timescale for the envelope that included an assumption of mass loss due to outflow from the central protostar. We do not include outflows in any way in these models. The lack of outflows in this work has two implications: 1) the mass evolution, as depicted in Figure 2, is incomplete and 2) we do not consider the effects of an evacuated outflow cavity. Fortunately, the mass evolution is not considerably altered by the exclusion of outflows. Calvet (1998) found that the ratio of mass loss rate to mass accretion rate is  $\sim 0.1$ . We are unable to model the scattered light coming from the outflow cavity. Others have, however, and we discuss their work in Section 7.4.

M98 also assume the envelope to have a density profile with a free-falling structure,  $n(r) \propto r^{-3/2}$ . We use the Shu77 solution, which has an inner free-falling envelope surrounded by a static envelope with  $n(r) \propto r^{-2}$ . These differences in structure of the envelope cause great disparities in the opacity. For example, a core that has  $0.8 M_{\odot}$  of material with  $n(r) \propto r^{-3/2}$  creates  $\tau_{\nu}(100\mu\text{m}) = 0.26$ . A core with the same amount of material but described by the Shu77 collapse solution, with an infall radius that is one-half of the outer radius, creates  $\tau_{\nu}(100\mu\text{m}) = 0.17$ . Such a disparity causes large changes in  $T_{bol}$ . For example, if we place a  $0.7 L_{\odot}$  star with  $T_{eff}=2000$  K inside these two cores, the Shu77 core has  $T_{bol} = 416$  K, and the free-falling core has a bolometric temperature that is half as high,  $T_{bol} = 207$  K.

M98 do not calculate the full SED. Instead, they consider the optically thin and thick limits and calculate two moments of the protostellar spectrum: the bolometric temperature and luminosity. On the other hand, we use DUSTY to calculate the full radiative transfer in the protostellar system.

Finally, M98 use a single power-law to describe the dust emissivity,  $\kappa$ . In contrast, we use the dust properties calculated by Ossenkopf & Henning (1994). While the dust opacity is aptly described by a power-law at long wavelengths, the shorter wavelength opacities are clearly not properly represented in the same way (see Figure 1).

Interestingly, the data encompass both models, but M98's models obviously best cover the median range for the data. However, there are a substantial number of sources that have a lower bolometric luminosity than either model allows. Perhaps, these sources are in the quiescent stage of episodic accretion so that  $L_{acc}$  is very low, or these low-luminosity objects could simply have a mass

less than  $0.3 M_{\odot}$  and not be included in these models. Also, our models show higher luminosities at later times than most of the data, a result of the aforementioned "luminosity problem." Perhaps, accretion does occur episodically and only for short times, and we should expect only a few objects to be in the phase where material is accreting onto the star and, hence, have a high luminosity. Another explanation, of course, is that the assumption of constant accretion throughout the star's evolution is wrong.

#### 7.4. Infrared Color-Magnitude Diagrams

In Figure 20, we show color-magnitude diagrams as would be observed with the Multiband Imaging Photometer for Spitzer (MIPS) on the Spitzer Space Telescope (SST). The three mass sequences ( $0.3, 1.0$ , and  $3.0 M_{\odot}$ ) are represented by the black lines in these figures. We show the magnitude at  $24 \mu\text{m}$  ([24]) plotted against the  $[24] - [70]$  color; on the right of Figure 20, we plot  $[70]$  and  $[70] - [160]$ .

Also, we show the models of W03 from Figure 8a of their work. The colored lines show W03's calculations over varying angles of inclination. The magenta line represents almost all inclination angles for the Class 0 stage, and the magenta triangle is the Class 0 stage as viewed pole-on.

Many differences exist between these models and our work. For example, W03 describe the envelope as a rotating, freely falling envelope (Ulrich 1976); W03 also set the envelope's inner radius to be quite small ( $\sim 10R_{\odot}$ ) while we use a much larger inner radius. In addition, W03 have a number of "common" model parameters, which do not change for the different models. These parameters include the stellar radius, temperature, and mass as well as the overall source luminosity. In our model, we allow all of these to evolve with time. Finally, W03 included the effects of outflow cavities, 2-dimensional disks, and varying inclination angles. We are unable to account for these things.

Young objects in the PPC/Class 0 segment of their lifespan are very red in our calculations and occupy the lower, right-hand section of this plot. However, these models are bluer in this plane than the W03 models for a Class 0 source. Several factors probably contribute to this disparity. Most of the difference arises from the fact that W03's models have a considerably more luminous central source than our models. Thus, the envelope material is heated more and emits a greater  $70 \mu\text{m}$  flux. Because W03 uses a very small inner radius, the optical depth is larger than for our models even though they may have similarly massive envelopes. Therefore, relative to the  $24 \mu\text{m}$  flux, there is a higher  $70 \mu\text{m}$  flux for W03's models, and their Class 0 stage appears redder (and, of course, more luminous). The effect is much less pronounced in the  $[70] - [160]$  plane because these longer wavelength fluxes are less affected by optical depth effects.

As with W03's models, our evolutionary tracks show that the objects become bluer in the  $[24] - [70]$  color as the source becomes more luminous and  $[24]$  increases. We have marked the PPC/Class 0 and Class 0/I transitions (as determined by  $L_{bol}/L_{smm}$  as in section 7.2). The Class I/II transition occurs at the end of our modeling sequence when all envelope mass has accreted onto

the star and disk. However, aspherical effects are most relevant with these later stages, so these models probably underestimate the 24  $\mu\text{m}$  flux for the Class I/II transition. Transitions for the 0.3  $M_\odot$  models are shown as cyan squares, the red squares represent the transitions for the 1  $M_\odot$  model, and the green squares are for the 3.0  $M_\odot$  model.

The right panel of Figure 20 shows a simpler behavior for the evolution as seen at 70 and 160  $\mu\text{m}$ . As an FHC, the protostar appears very red but becomes bluer as the core collapses to  $\sim 3 R_\odot$  and grows in luminosity. The 160  $\mu\text{m}$  flux increases over time as the internal luminosity continues to grow. However, there is a point where the envelope contains so little material that the 160  $\mu\text{m}$  flux drops despite the fact that the far-infrared emission of the internal star is growing. By the end of these tracks, the objects have reached the end of their Class I stage; they no longer have envelope material but do have an optically thick disk.

## 8. CONCLUSIONS

We have presented the results from modeling the evolution of protostars with 3 different masses: 0.3, 1.0, and 3.0  $M_\odot$ . The framework for the evolution of these protostars was taken mostly from the work of Adams & Shu (1986) but also used the results from several other authors. These efforts were similar and complementary to the work of Myers et al. (1998) and Whitney et al. (2003) but employed different methods and theories and, hence, got different results.

We note that the evolution of these modeled protostars is significantly affected by the existence and lifetime of the first hydrostatic core. The work done heretofore is useful (Boss & Yorke 1995; Masunaga et al. 1998), but more detailed theoretical work is needed. As we begin to observe earlier stages of star formation (Young et al. 2004a), the role of the FHC must be ascertained.

We find that the Class 0 stage, when determined by

$T_{bol}$ , should be short-lived, lasting only about 1/10 to 1/4 of the protostar's life. This result is somewhat model dependent, but it should also extend to other models of star formation. Therefore, the surveys being conducted with the Spitzer Space Telescope and 2MASS should reveal a small fraction of Class 0 to Class I objects. However, we suggest not using the  $T_{bol}$  criterion for classification.

We find that the bolometric temperature is a poor discriminator for protostars at early evolutionary stages. Instead, we suggest using the  $L_{bol}/L_{smm}$  signature proposed by André et al. (1993). Based on physical grounds, we suggest these boundaries for classifying protostars:  $L_{bol}/L_{smm} = 35$  for PPC/Class 0,  $L_{bol}/L_{smm} = 175$  for Class 0/I, and  $L_{bol}/L_{smm} \sim 2000$  for the Class I/II transition. The latter is largely dependent on the adopted disk model. Also,  $L_{bol}/L_{smm}$  is not relevant after all envelope mass has been accreted (beyond the Class I stage) since it is a measure of the stellar to envelope mass ratio (André et al. 1993).

We have presented several observational tools by which the inside-out collapse model can be effectively tested: infrared color-magnitude diagrams, plots of the bolometric luminosity and temperature, and a plot of  $T_{bol}$  and  $L_{bol}/L_{smm}$ . Large surveys will produce these observable quantities for hundreds of young protostars and test the theory of inside-out collapse.

## 9. ACKNOWLEDGEMENTS

We thank Minho Choi for the use of his program to calculate the density profiles. Also, many thanks to Moshe Elitzur, Maia Nenkova, and Zeljko Ivezić for providing the modified version of DUSTY that allows heating by the ISRF and for much assistance in the use of DUSTY. Many thanks also to our anonymous referee whose thorough reading and thoughtful critique have made this a better paper. This work is supported by NASA grants NAG5-10488 and NNG04GG24G.

## REFERENCES

André P., & Montmerle, T., 1994, ApJ, 420, 837  
 André P., Ward-Thompson, D., & Barsony, M., 1993, ApJ, 406, 122  
 Adams, F.C. & Shu, F.H., 1986, ApJ, 308, 836  
 Adams, F.C., Shu, F.H., Lada, C.J., 1988, ApJ, 326, 865  
 Adams, F.C., Lada, C.J., & Shu, F.H., 1987, ApJ, 312, 788  
 Alexander, D.R., Augason, G.C., & Johnson, H.R., 1989, ApJ, 345, 1014  
 Benjamin, R.A., et al. 2003, PASP, 115, 953  
 Boss, A.P. & Yorke, H.W., 1995, ApJ, 439, L55  
 Boyd, D.F.A. & Whitworth, A.P., 2005, A&A, 430, 1059  
 Butner, H.M., Natta, A., & Evans, N.J. II, ApJ, 420, 326  
 Calvet, N., 1998, in AIP Conf. 431, ed. S.S. Holt and T.R. Kallman (Woodbury, NY:AIP Press), pp. 495-504  
 Chen, H., Grenfell, T.G., Myers, P.C., & Hughes, J.D., ApJ, 478, 295  
 Chen, H., Myers, P.C., Ladd, E.F., & Wood, D.O.S., ApJ, 445, 377  
 Chiang, E.I. & Goldreich, P., 1997, ApJ, 490, 368  
 D'Antona, F. & Mazzitelli, I., 1994, ApJS, 90, 467 (DM)  
 Doty, S.D., Everett, S.E., Shirley, Y.L., Evans, N.J. II, & Palotti, M.L., 2005, MNRAS, accepted, astro-ph/0501676  
 Draine, B.T. & Lee, 1984, ApJ, 285, 89  
 Evans, N.J. II, Rawlings, J.M.C., Shirley, Y.L., & Mundy, L.G., 2001, ApJ, 557, 193  
 Evans, N.J. II, et al., 2003, PASP, 115, 965  
 Froebrich, D., 2005, ApJS, 156, 169  
 Goodman, A.A., Benson, P.J., Fuller, G.A., & Myers, P.C., 1993, ApJ, 406, 528  
 Hogerheijde, M.R., Sandell, G., 2000, ApJ, 534, 880  
 Ivezić, Ž. & Elitzur, M., 1997, MNRAS, 287, 799  
 Ivezić, Ž., Nenkova, M., & Elitzur, M., 1999, astro-ph/9910475  
 Kenyon, S.J. & Hartmann, L., 1995, ApJS, 101, 117  
 Kenyon, S.J. & Hartmann, L., 1987, ApJ, 323, 714  
 Kitamura, Y., Momose, M., Yokogawa, S., Kawabe, R., Tamura, M., & Ida, S., 2002, ApJ, 581, 357  
 Larson, R.B., 1969, MNRAS, 145, 271  
 Lee, J.-E., Bergin, E.A., & Evans, N.J. II, 2004, ApJ, 617, 360  
 Li, Z.-Y., 2002, ApJ, 574, L159  
 Masunaga, H. & Inutsuka, S.-I., 1999, ApJ, 510, 822  
 Masunaga, H., Miyama, S.M., & Inutsuka, S.-I., 1998, ApJ, 495, 346  
 Motte, F. & André, P., 2001, A&A, 265, 440  
 Motte, F., André, P., & Neri, R., 1998, A&A, 336, 150  
 Mundy, L.G., Looney, L.W., Erickson, W., Grossman, A., Welch, W.J., Forster, J.R., Wright, M.C.H., Plambeck, R.L., Lugten, J., & Thornton, D.D., 1996, ApJ, 464, L169  
 Myers, P.C. & Ladd, E.F., 1993, ApJ, 413, L47.  
 Myers, P.C., Adams, F.C., Chen, H., & Schaff, E., 1998, ApJ, 492, 703 (M98)  
 Osseenkopf, V. & Henning, T. 1994, A&A, 291, 943  
 Padgett, D.L., Brandner, W., Stapelfeldt, K.R., Strom, S.E., Terebey, S., & Koerner, D., 1999, AJ, 117, 1490  
 Palla, F. & Stahler, S.W., 1991, ApJ, 375, 288  
 Pendleton, Y. J., Tielens, A. G. G. M., & Werner, M. W., 1990, ApJ, 349, 107  
 Pollack, J.B., Hollenbach, D., Beckwith, S., Simonelli, D.P., Roush, T., & Fong, W., 1994, ApJ, 421, 615

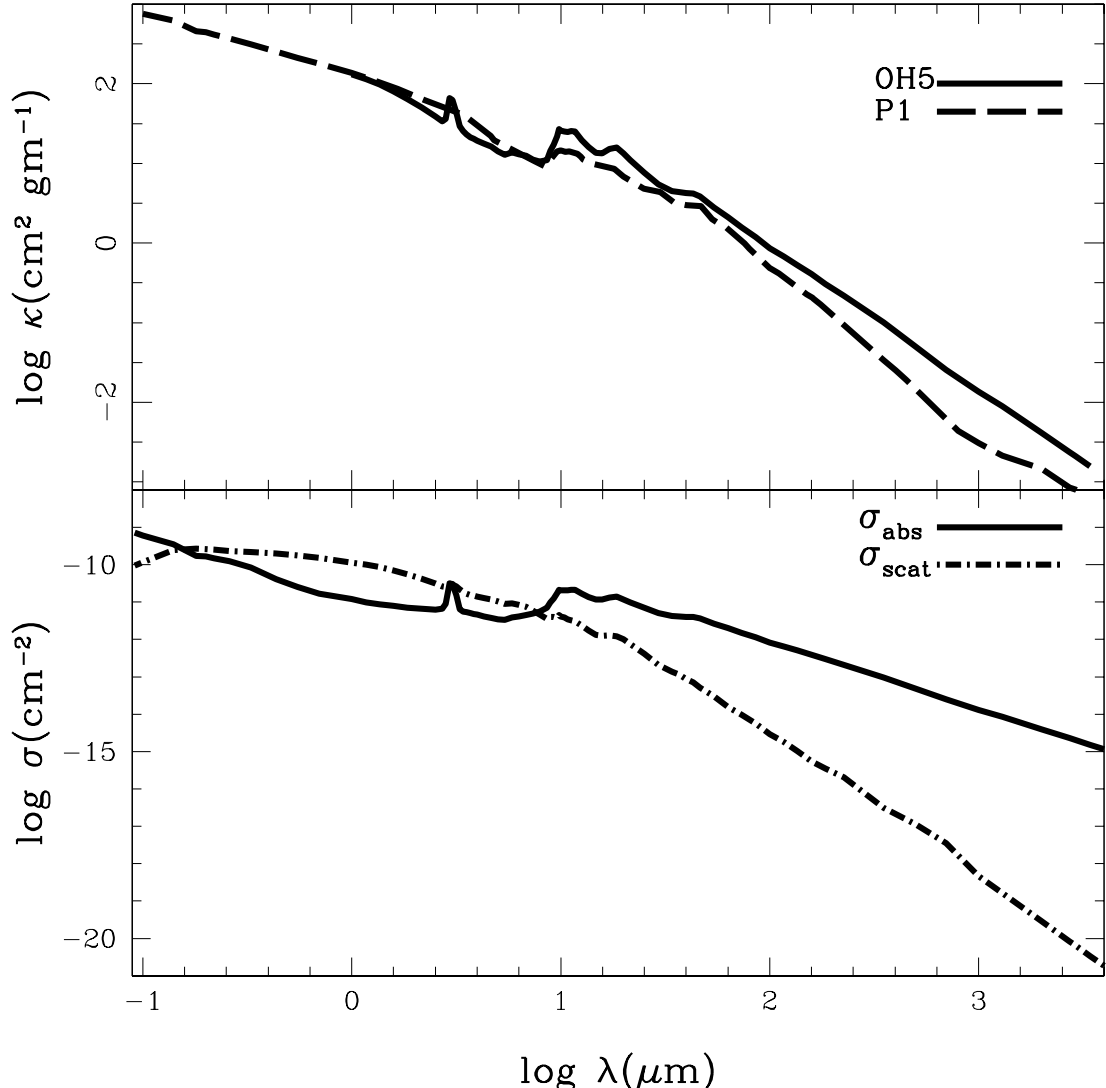


FIG. 1.— The top plot shows the opacity of the gas with OH5 and P1 dust (assuming a gas-to-dust ratio of 100). We have used the OH5 dust for our models. However, we used the P1 opacities for wavelengths shortward of  $1 \mu\text{m}$ . The bottom plot shows the absorption and scattering cross-sections for OH5 dust.

Shirley, Y.L., Evans, N.J. II, & Rawlings, J.M.C., 2002, *ApJ*, 575, 337  
 Shirley, Y.L., Evans, N.J. II, Rawlings, J.M.C., & Gregersen, E.M., 2000, *ApJS*, 131, 249  
 Shirley, Y.L., Nordhaus, M.K., Grcevich, J.M., Evans, N.J. II, Rawlings, J.M.C., & Tatematsu, K., 2004, *ApJ*, submitted  
 Shu, F.H., 1977, *ApJ*, 214, 488 (Shu77)  
 Stahler, S.W., 1983, *ApJ*, 274, 822  
 Tafalla, M., Mardones, D., Myers, P.C., Caselli, P., Bachiller, R., & Benson, P.J., 1998, *ApJ*, 504, 900  
 Terebey, S., Shu, F.H., & Casen, P. 1984, *ApJ*, 286, 529  
 Ulrich, R.K., 1976, *ApJ*, 210, 377  
 Visser, A.E., Richer, J.S., Chandler, C.J., 2002, *AJ*, 124, 2756  
 Ward-Thompson, D., Scott, P.F., Hills, R.E., & André, P., 1994, *MNRAS*, 268, 276  
 White, R. & Hillenbrand, L., 2004, *ApJ*, 616, 998  
 Whitney, B.A., Wood, K., Bjorkman, J.E., & Cohen, M., 2003, *ApJ*, 598, 1079  
 Young, C.H., et al., 2004a, *ApJS*, 154, 396  
 Young, K.E., et al., 2005, accepted *ApJ*  
 Young, K.E., Lee, J-E., Evans, N.J. II, Goldsmith, P.F., & Doty, S.D., 2004b, *ApJ*, 614, 252  
 Young, C.H., Shirley, Y.L., Evans, N.J. II, & Rawlings, J.M.C., 2003, *ApJS*, 145, 111  
 Zhou, S., Evans, N.J. II, Koempe, C., & Walmsley, C. M., 1993, *ApJ*, 404, 232

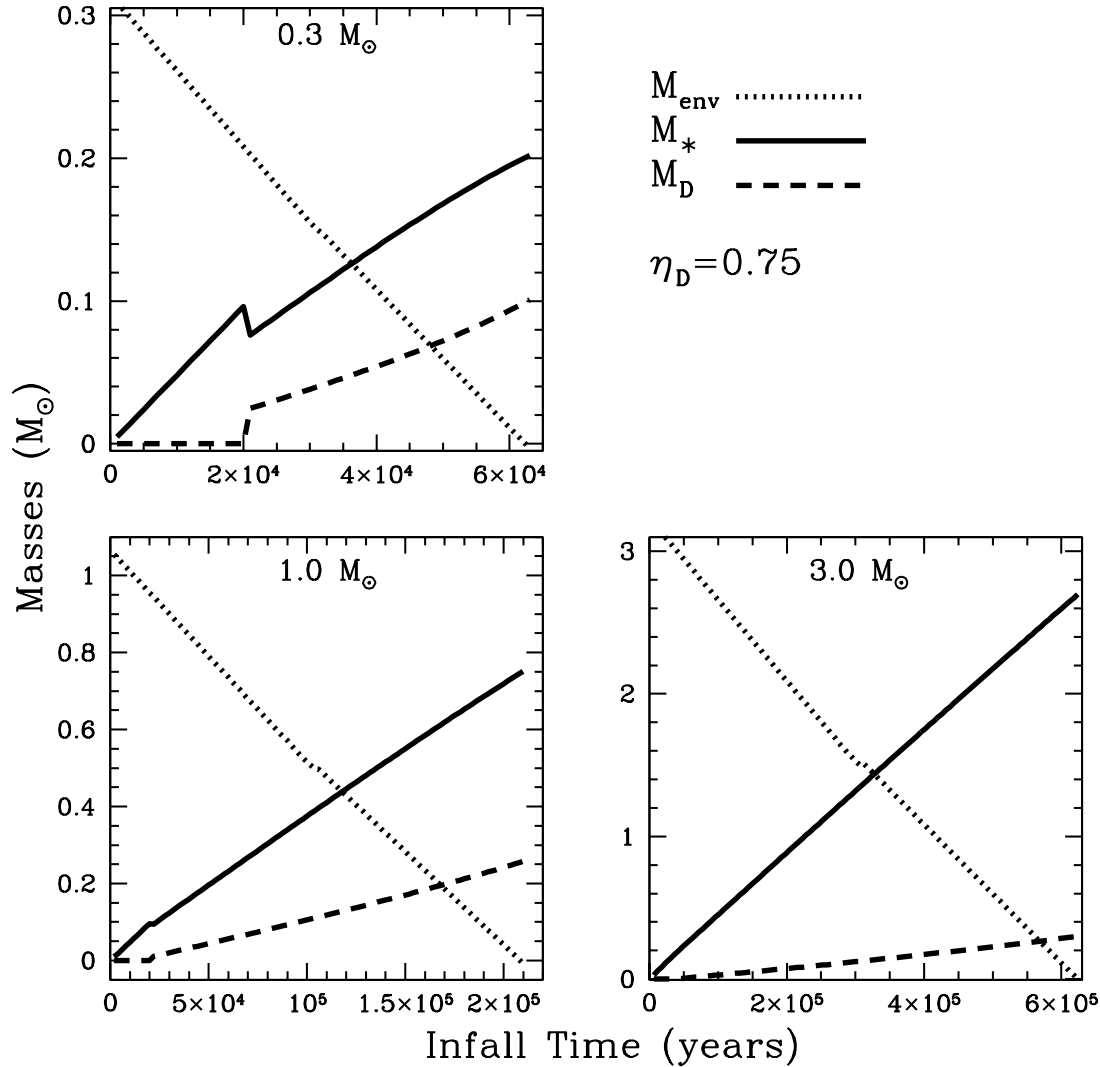


FIG. 2.— The mass of the star and disk increase as mass from the envelope is accreted by the protostellar system as shown here for the three mass scenarios considered.

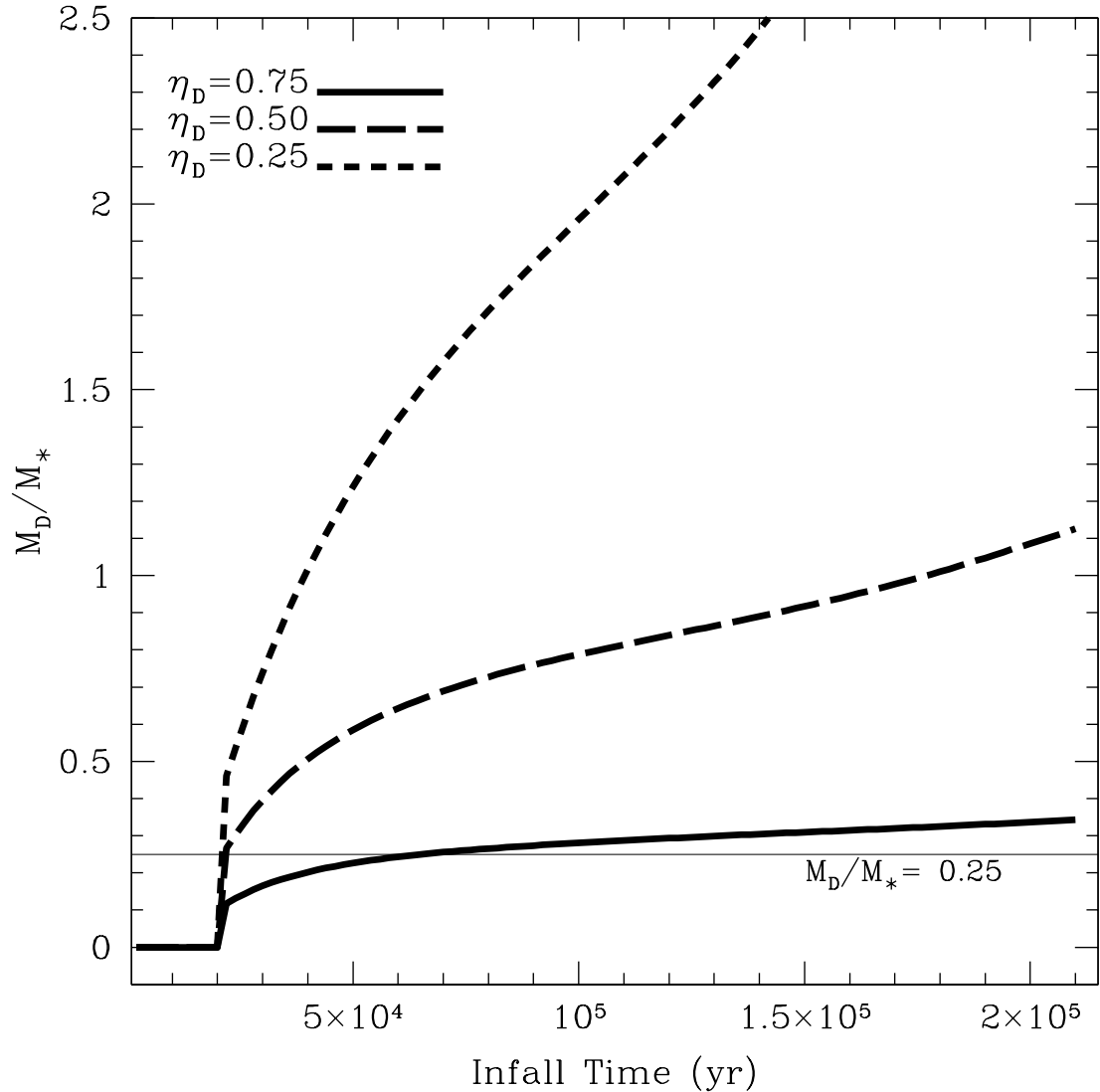


FIG. 3.— We show the ratio of disk to stellar mass for the  $1 M_{\odot}$  model as it evolves with time. We have chosen  $\eta_D = 0.75$  so that this ratio approaches 0.25. For the  $0.3$  and  $3.0 M_{\odot}$  models, we use  $\eta_D = 0.7$  and  $\eta_D = 0.9$ , respectively.

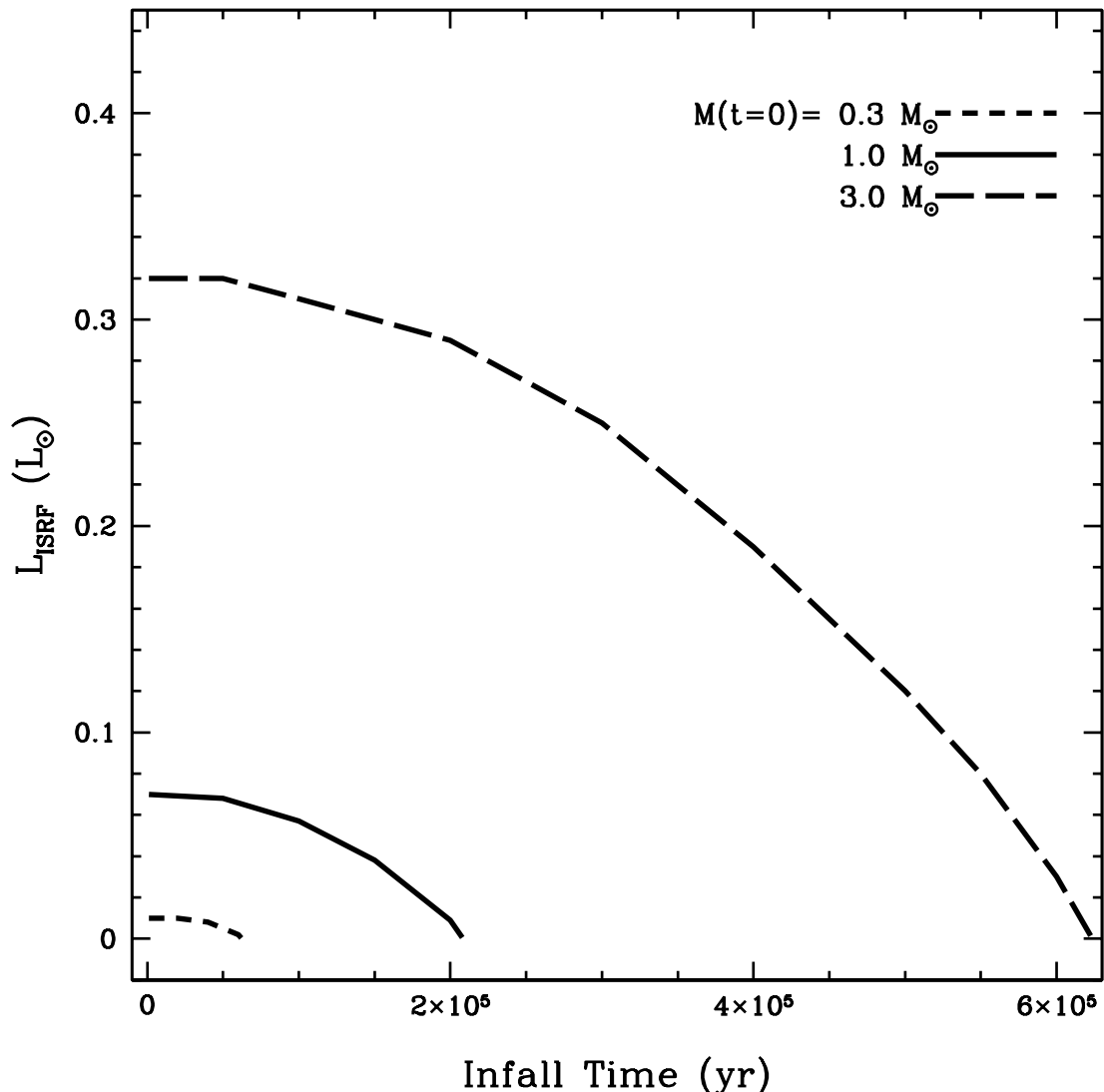


FIG. 4.— Evolution of the luminosity from the ISRF with time. Each line represents a core with a different initial mass.

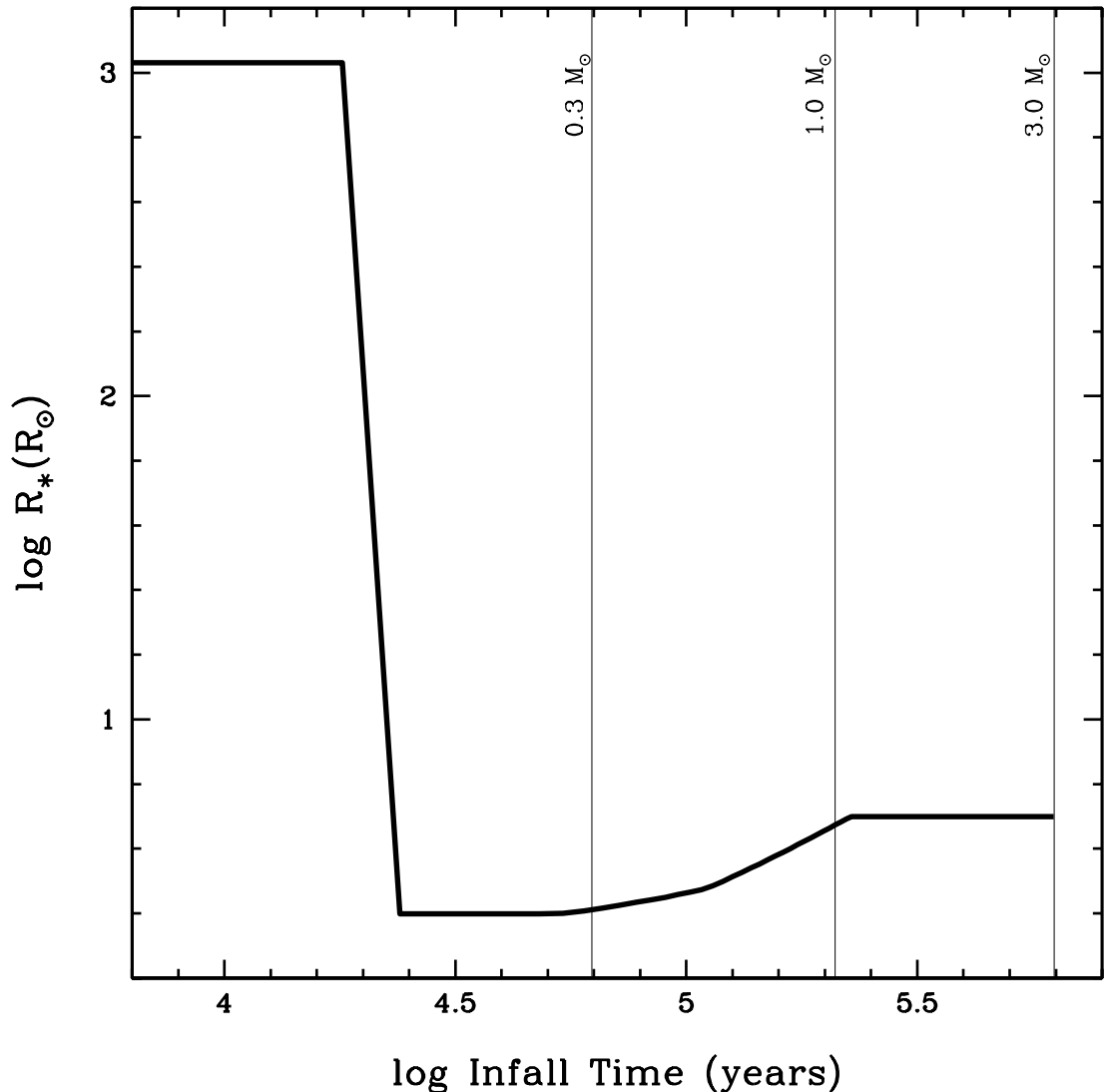


FIG. 5.— We show the data used for the radius of our evolving protostar. The radius in the first 20,000 years simulates the first hydrostatic core phase. The radius for the remaining time is from Figure 1 of Palla & Stahler (1991). The thin, vertical lines show where the evolution ends for the various masses modeled.

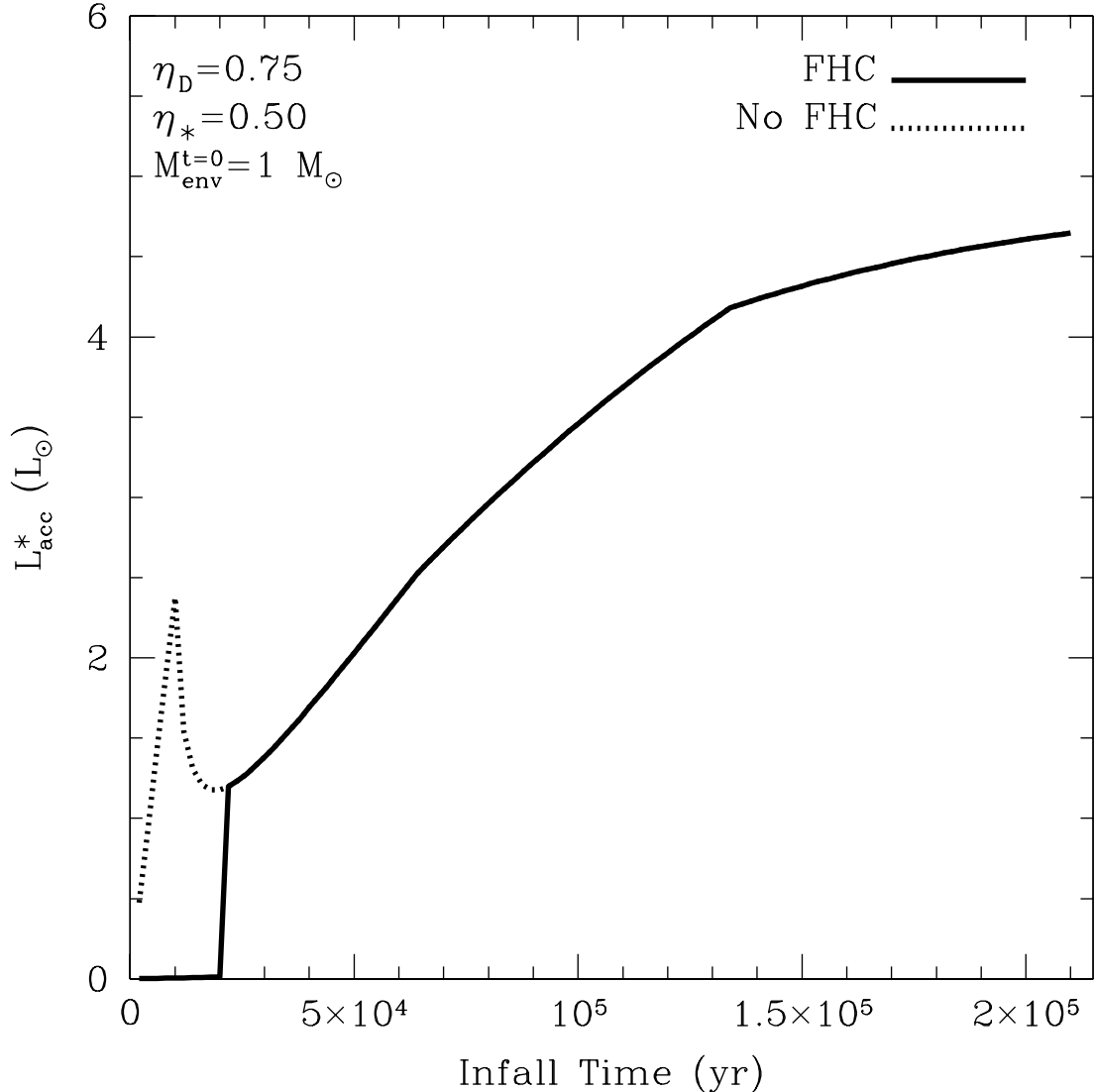


FIG. 6.— The solid line represents  $L_{acc}$  as it evolves with time; the first hydrostatic core (FHC) is included. Without the FHC,  $L_{acc}$  evolves as represented by the dotted line. For our models, we include the FHC.

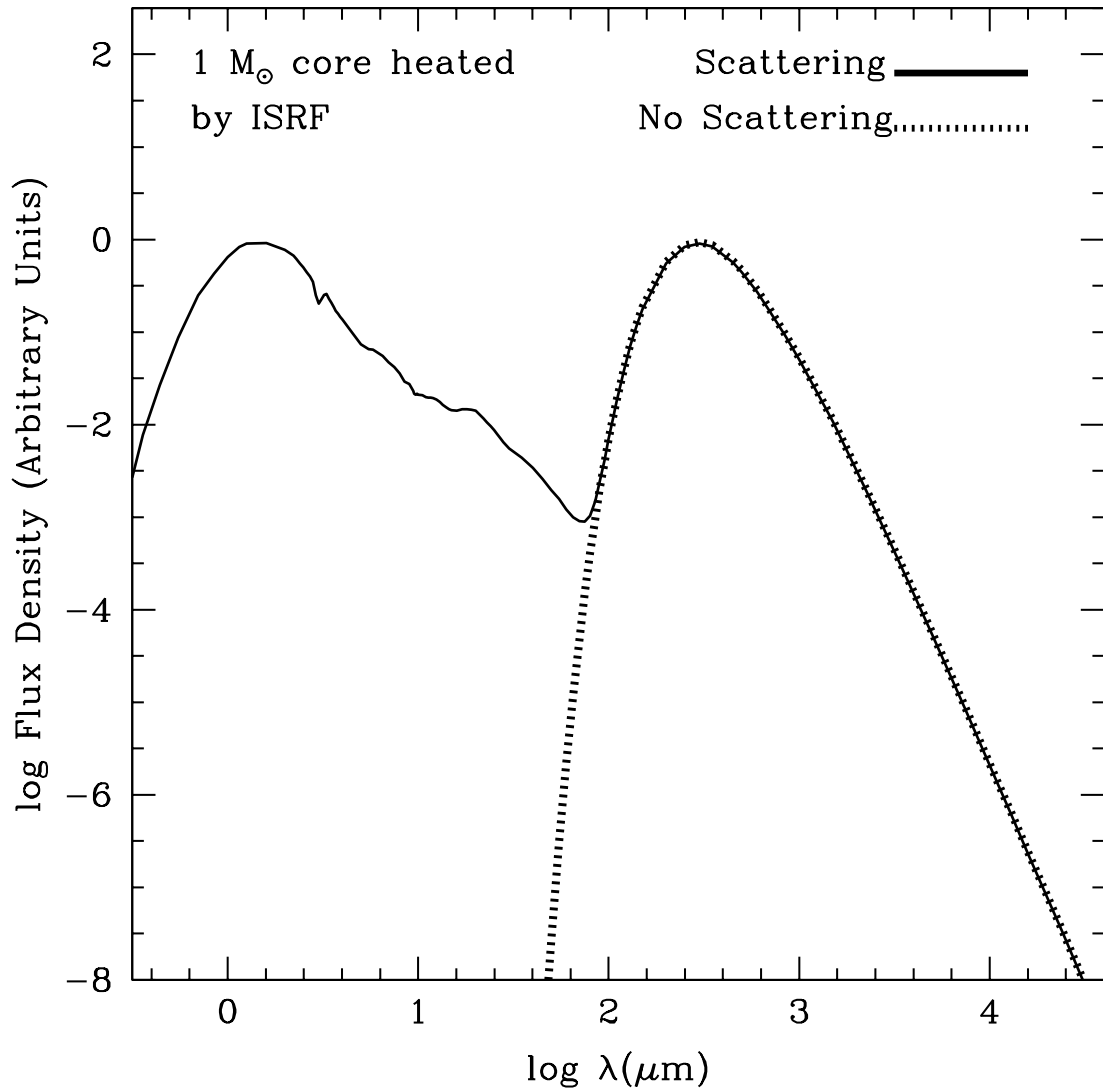


FIG. 7.— We plot the SED of a  $1 M_{\odot}$  core (with  $\tau_{100\mu\text{m}} = 1$ ). This model does not include a central luminosity source; the heating is entirely due to the ISRF. The solid line includes the effects of isotropic scattering while the dotted line does not.

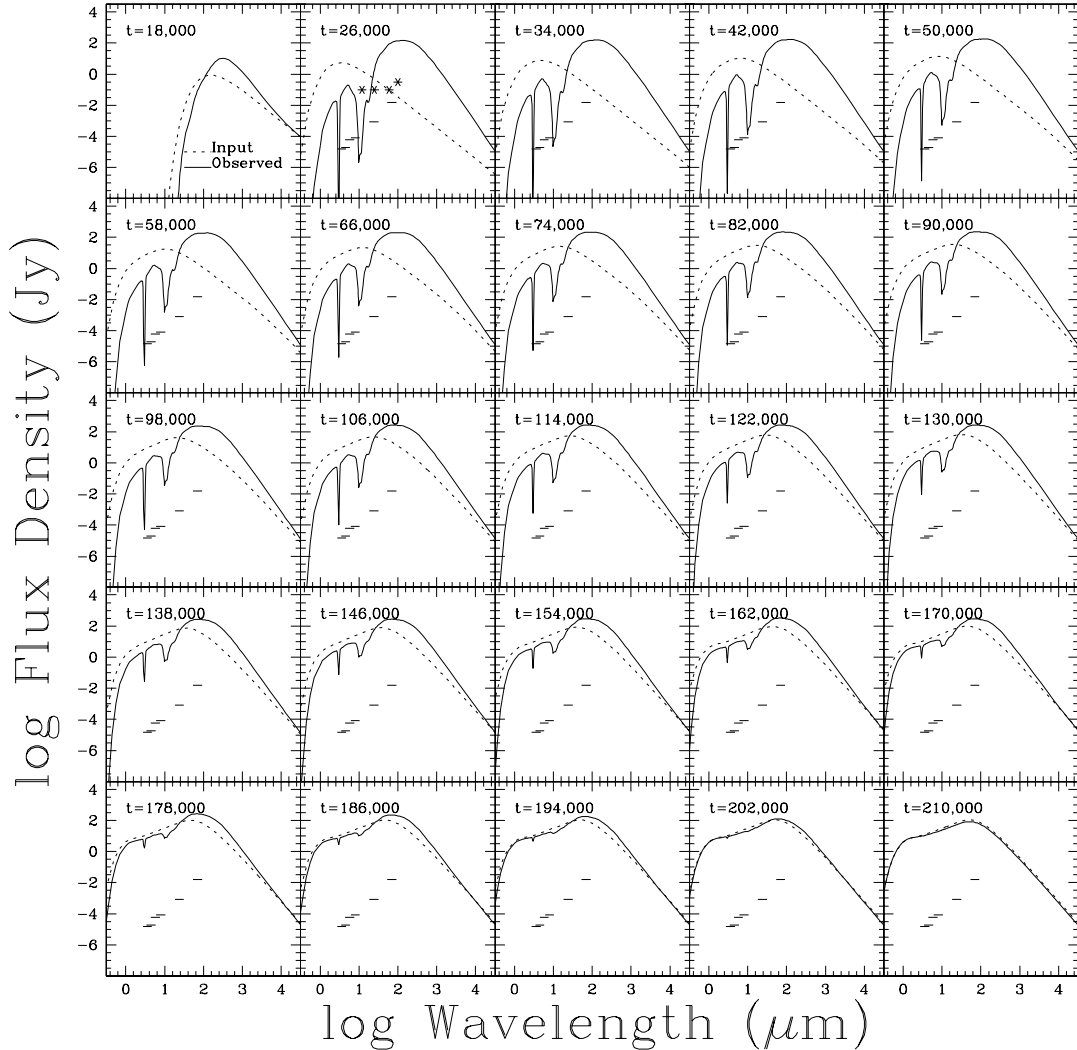


FIG. 8.— Each panel in the plot has the SED for a core with initial mass of  $1 M_{\odot}$ , a temperature of 10 K,  $\tau_{max} = 10$ ,  $\eta_D = 0.75$ , and  $\eta_* = 0.5$ . The age for the model is labeled in each panel. The dotted line is the input disk spectrum, and the solid line is the observed SED as calculated by DUSTY. Sensitivities for the Spitzer Cores to Disks Legacy program are shown as horizontal bars; IRAS sensitivities are in the second frame as asterisks. The distance is 140 pc.

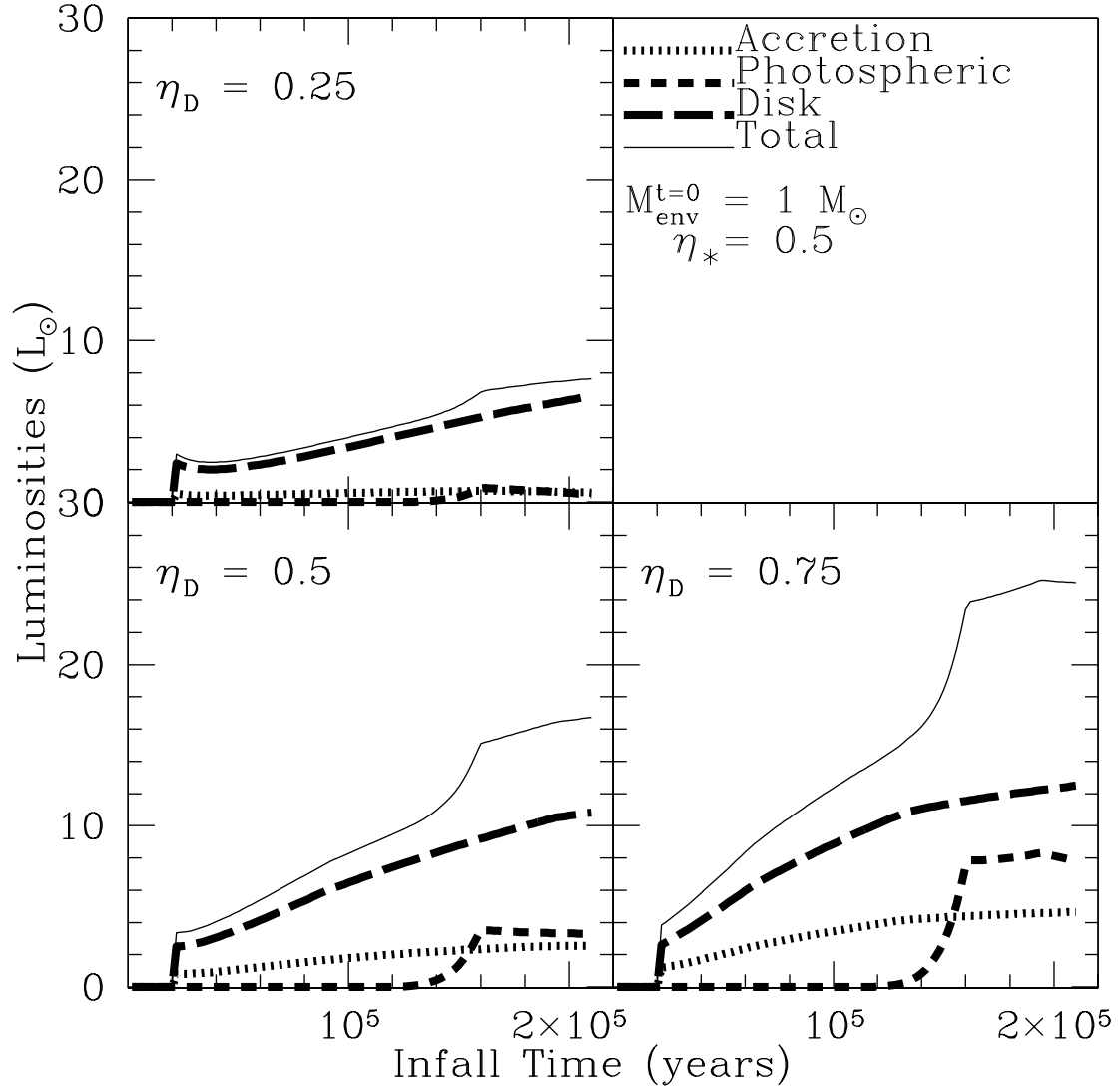


FIG. 9.— Contributing forms of luminosity are shown here for different values of  $\eta_D$ . The accretion luminosity ( $L_{acc}$ ) is from material accreting onto the star. Photospheric luminosity ( $L_{phot}$ ) is calculated by DM94 and due to contraction of the central star and deuterium burning. The disk luminosity ( $L_D$ ) has several components, which are described in section 2.3.3. The sum of these luminosities is shown by the “Total.”

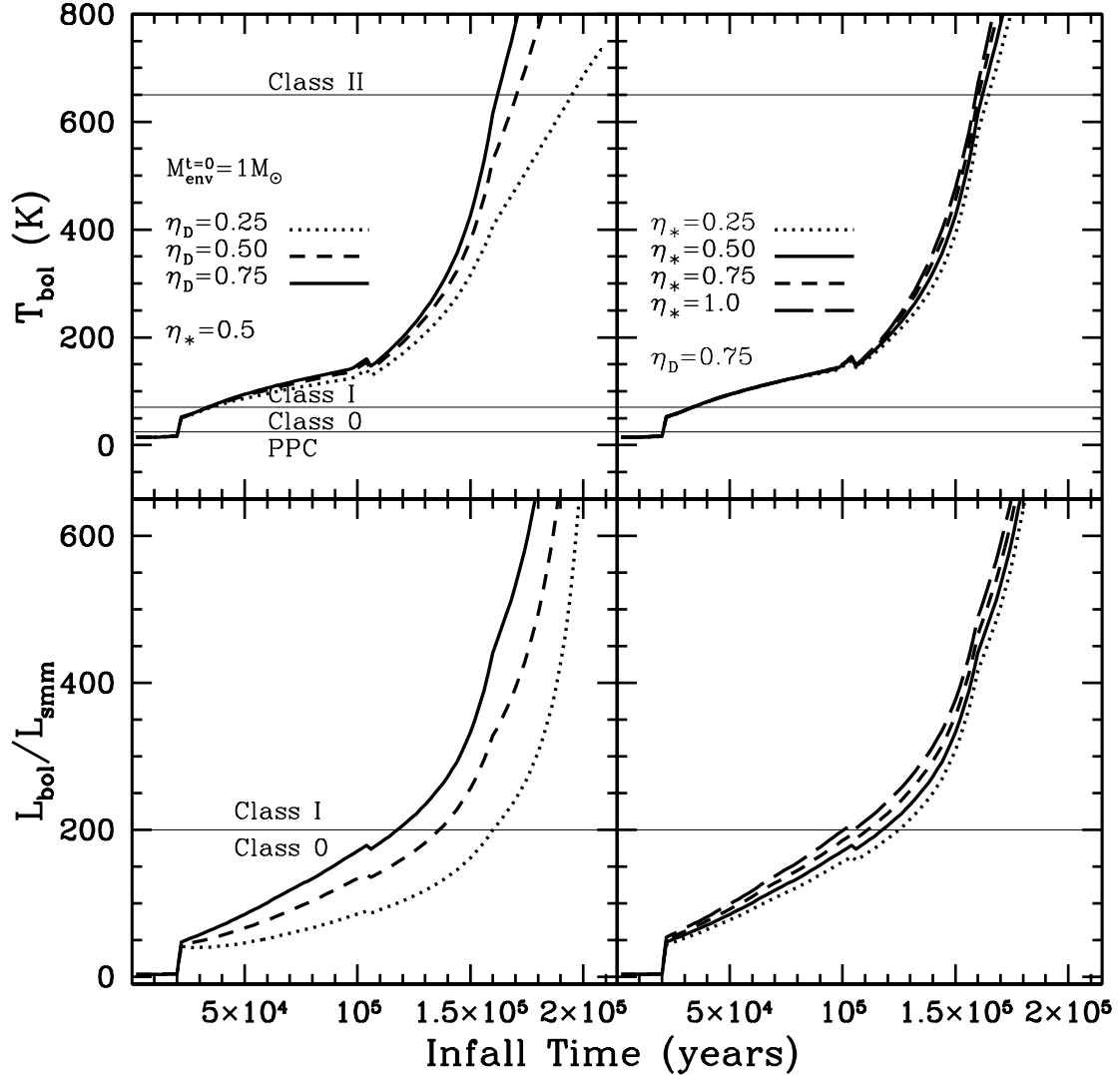


FIG. 10.— For the  $1 M_{\odot}$  core, we show  $T_{bol}$  and  $L_{bol}/L_{smm}$  with different values for  $\eta_D$  and  $\eta_*$ . The left panels show data where  $\eta_* = 0.5$  and  $\eta_D$  is varied; data in the right panels have  $\eta_D = 0.75$  and different values for  $\eta_*$ .

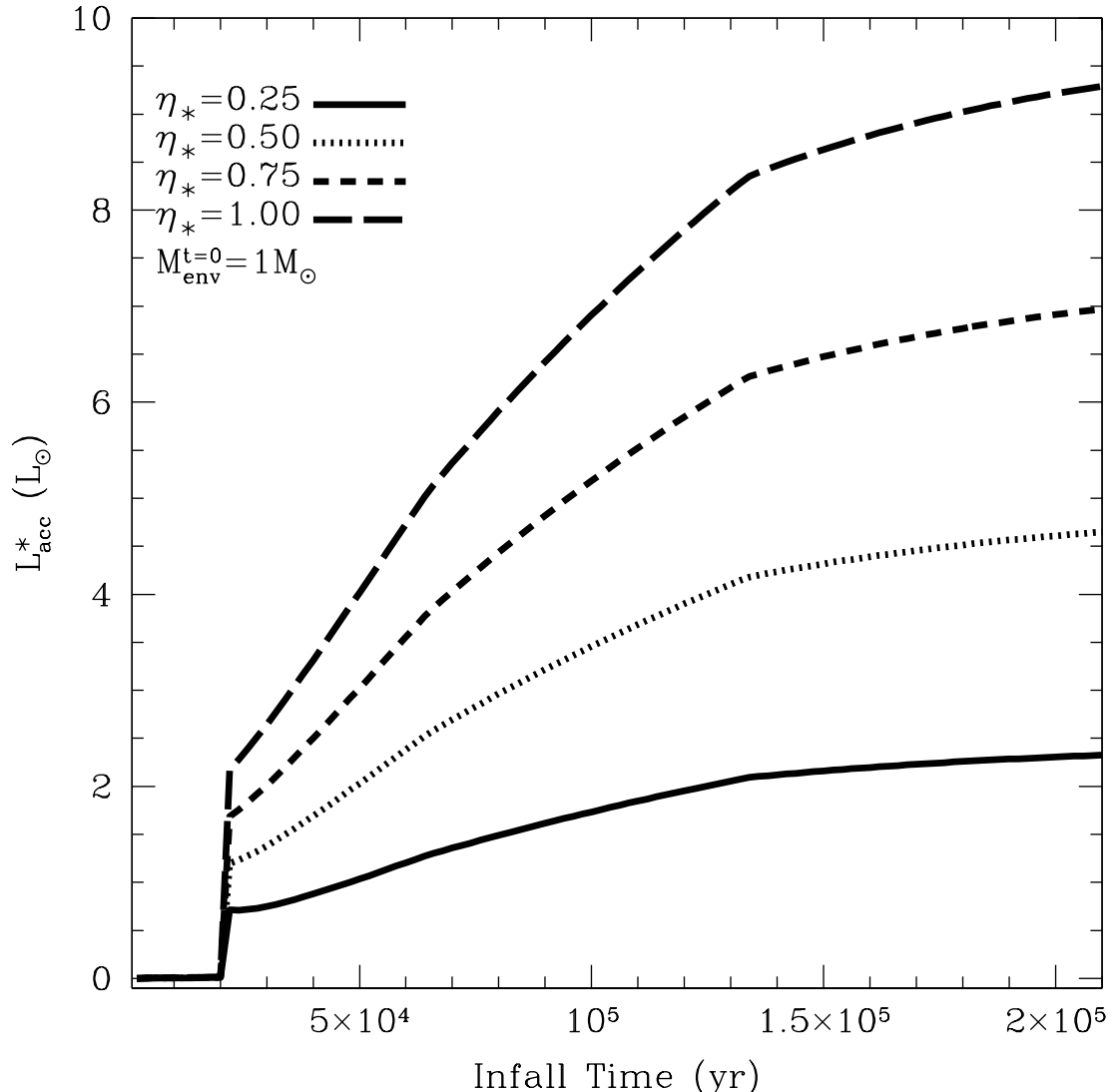


FIG. 11.— For the  $1 M_\odot$  core, we plot  $L_{acc}$  for various values of  $\eta_*$ . For our models, we choose  $\eta_* = 0.5$  in accord with Adams, Lada & Shu (1987).

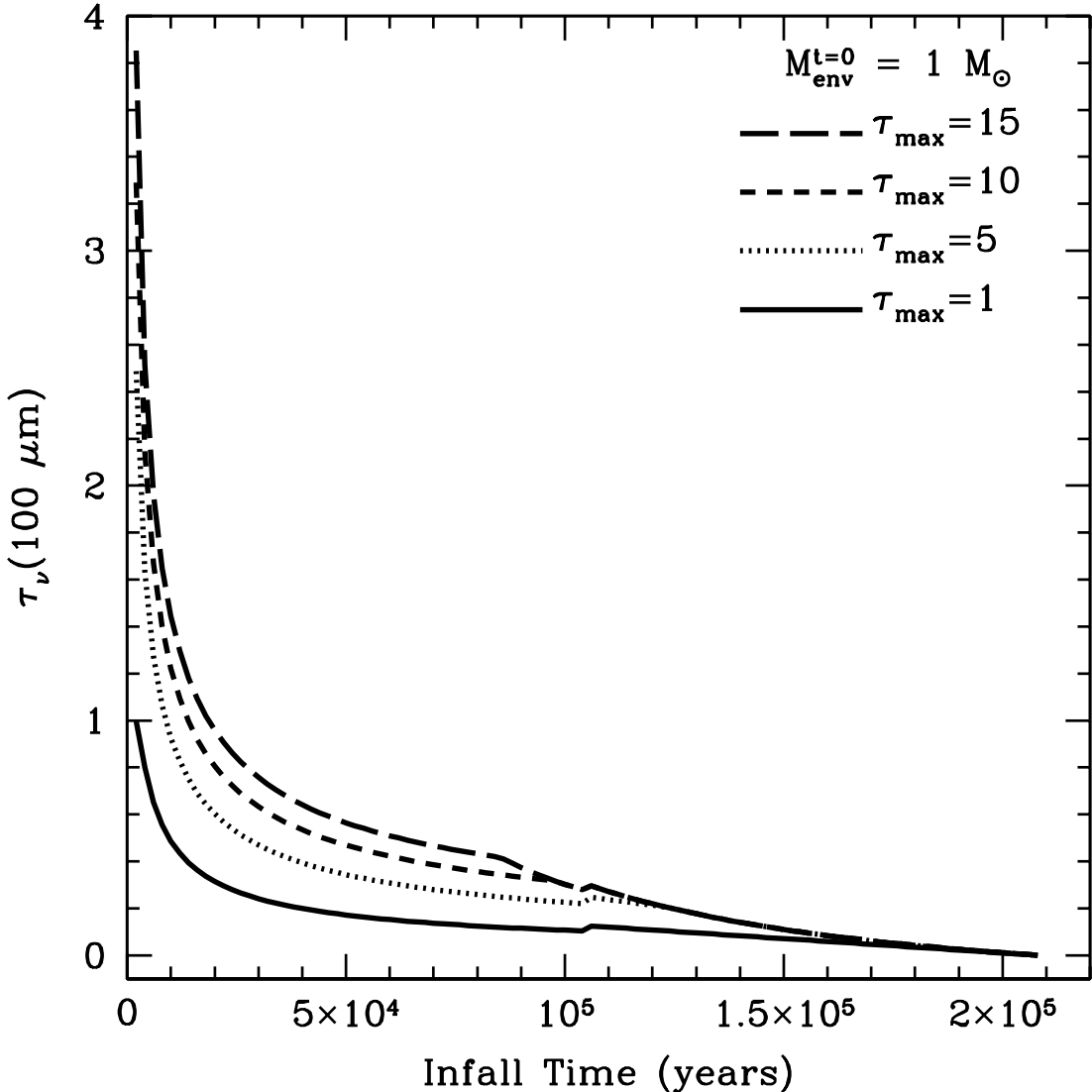


FIG. 12.— We set different initial conditions for the forming star by allowing  $\tau_\nu(100\mu\text{m})$  to range from 1 to 15. We vary  $\tau_\nu$  by changing the envelope's inner radius. There is a slight “kink” in the evolution of  $\tau_\nu$  around  $t = 10^5$  years that is due to the shift from the Shu77 collapsing envelope to a free-falling envelope with  $n(r) \propto r^{-3/2}$ .

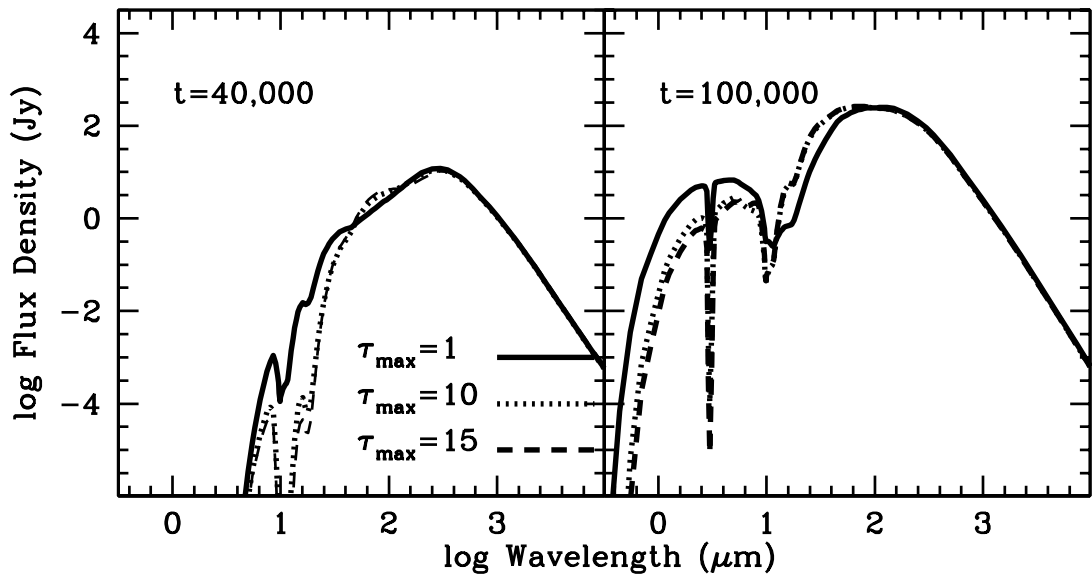


FIG. 13.— For the  $1 M_{\odot}$  core, we show the modeled SED with different values for  $\tau_{max}$ . The model with  $\tau_{max} = 1$  shows greater emission at short wavelengths than those with higher  $\tau_{max}$ . We choose  $\tau_{max} = 10$  for the models hereafter.

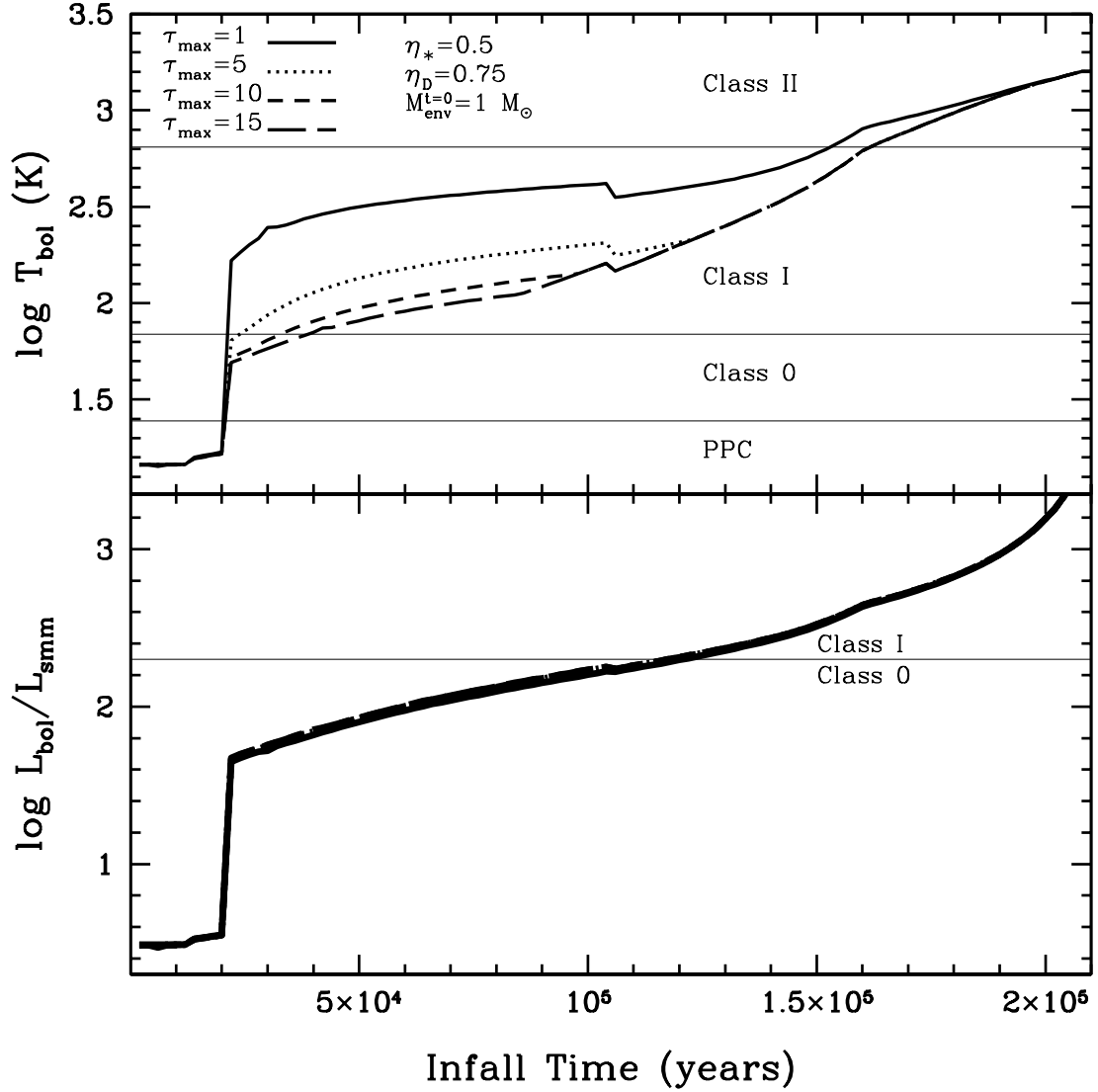


FIG. 14.— For the  $1 M_{\odot}$  core, we show  $T_{\text{bol}}$  and  $L_{\text{bol}}/L_{\text{smm}}$  with different values for  $\tau_{\text{max}}$ .

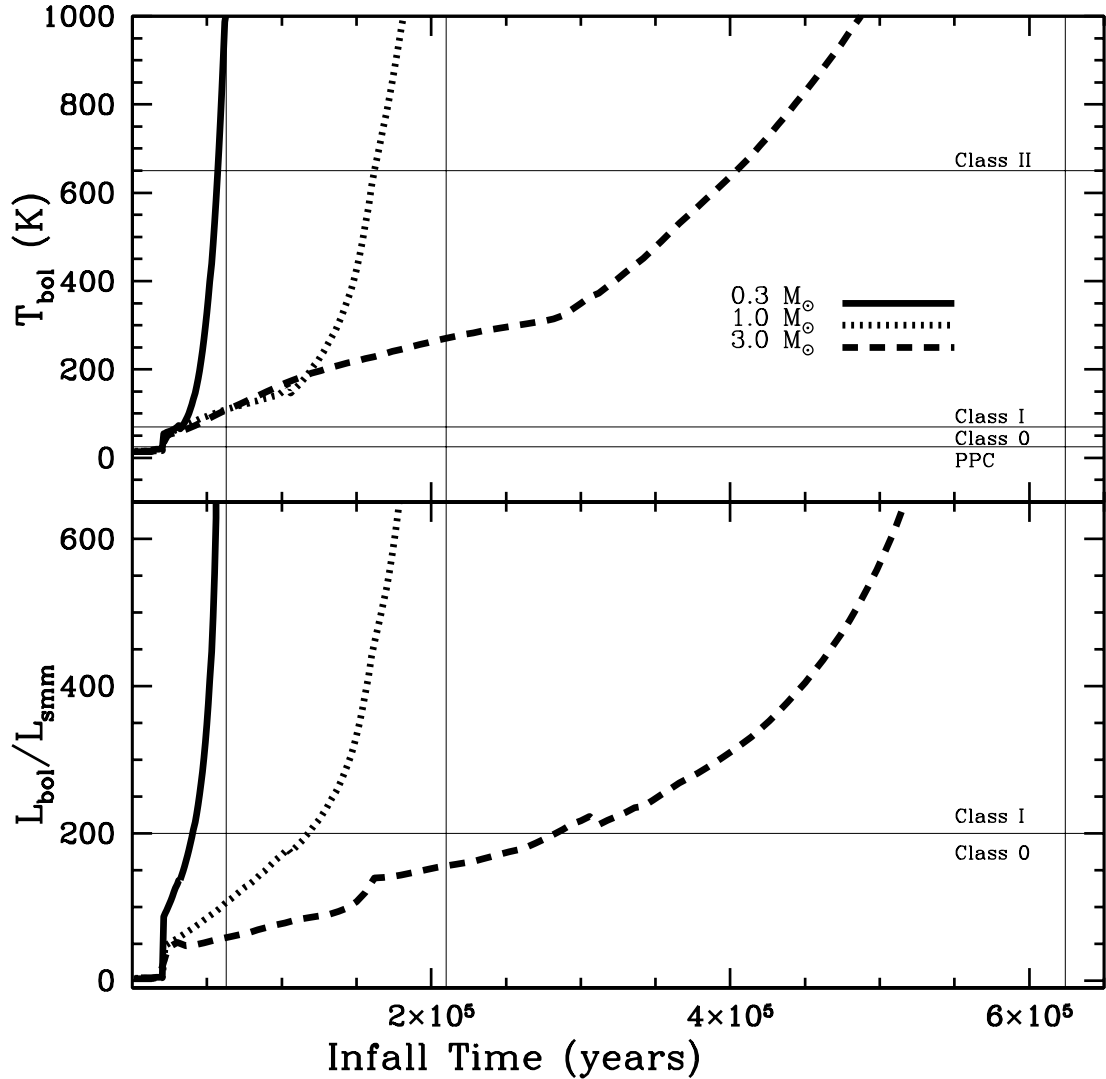


FIG. 15.— We plot  $T_{bol}$  and  $L_{bol}/L_{smm}$  as they evolve with time for each of the three models. The horizontal lines represent the boundaries for classes of protostars; vertical lines mark the point when all envelope material has accreted onto the star+disk system for each of the three modeled cores.

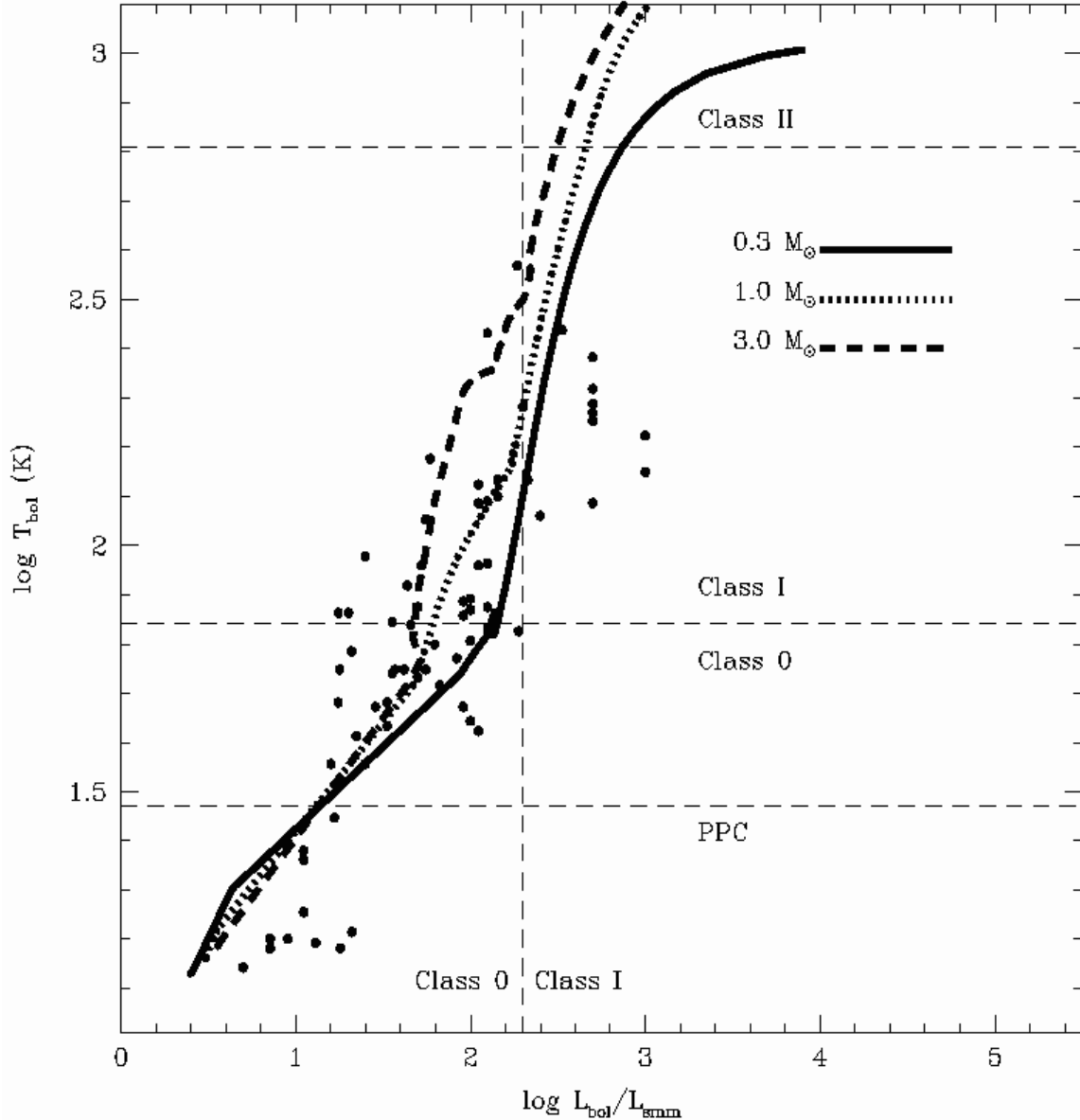


FIG. 16.— We plot  $T_{bol}$  and  $L_{bol}/L_{smm}$  for the three scenarios that we modeled. The points are data taken from Young et al. (2003), Shirley et al. (2002), Shirley et al. (2004), and Froebrich (2005).

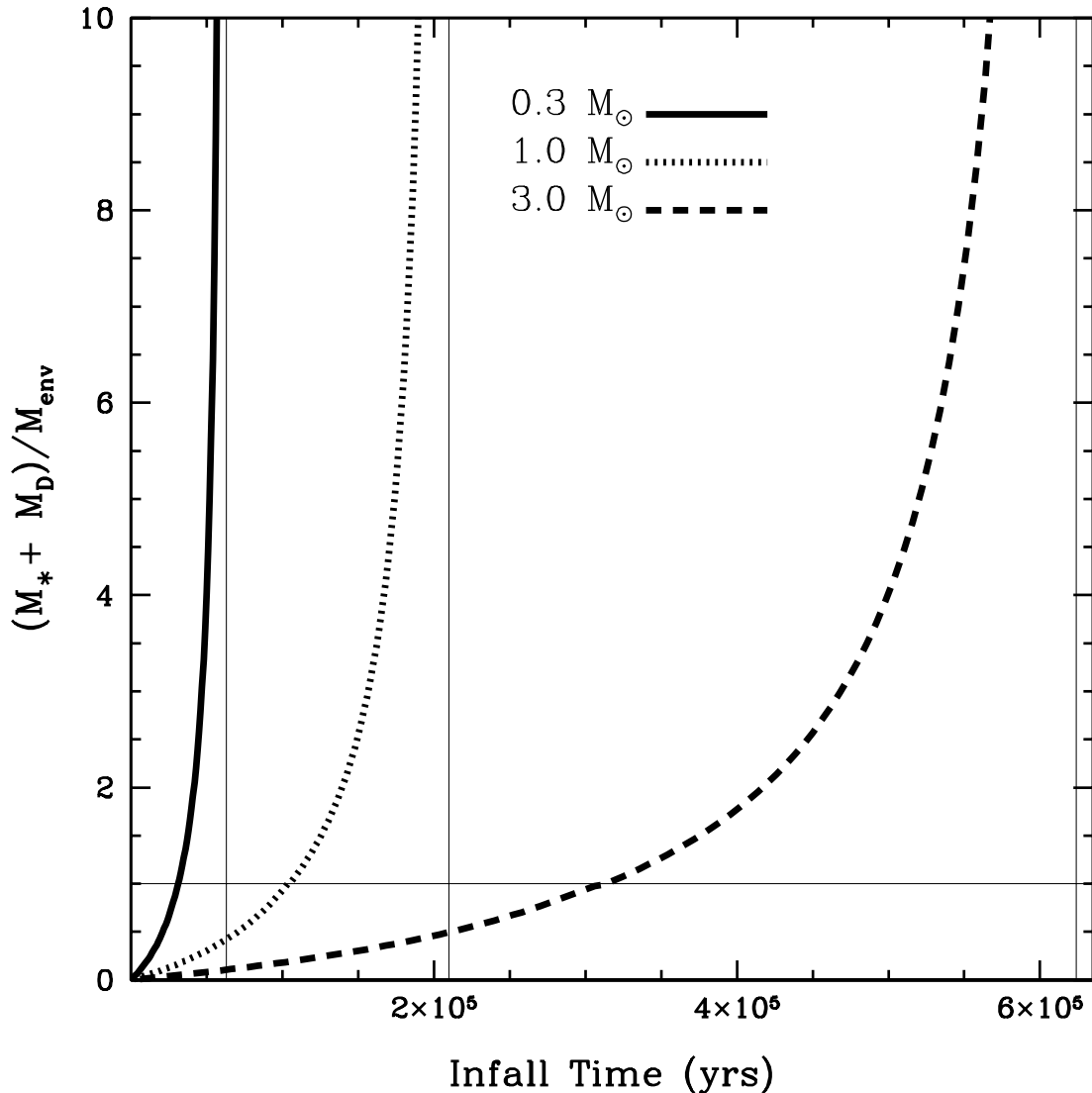


FIG. 17.— For the three models, we plot  $(M_* + M_D)/M_{env}$ . The thin, vertical lines mark the point when all of the envelope mass has accreted onto the star+disk system. The horizontal line shows where the envelope mass is equal to the accreted protostellar mass.

TABLE 1  
MODEL PARAMETERS

	Symbol	Adopted value
Envelope parameters		
Envelope inner radius	$r_i$	Equation 4
Envelope outer radius	$r_o$	Equation 1
Envelope dust opacity	$\kappa_\nu$	Ossenkopf & Henning (1994)
Disk parameters		
Inner radius	$R_i$	Equation 10
Outer radius	$R_o$	Equation 11
Accretion luminosity	$L_D$	Equation 33b, Adams & Shu (1986)
Temperature power-law	$T_D$	Equation 14
Stellar parameters		
Accretion luminosity	$L_{acc}$	Equation 33a, Adams & Shu (1986)
Photospheric luminosity	$L_{phot}$	D'Antona & Mazzitelli (1994)
Effective temperature	$T_{eff}$	Equation 19
Radius	$R_*$	Palla & Stahler (1991)

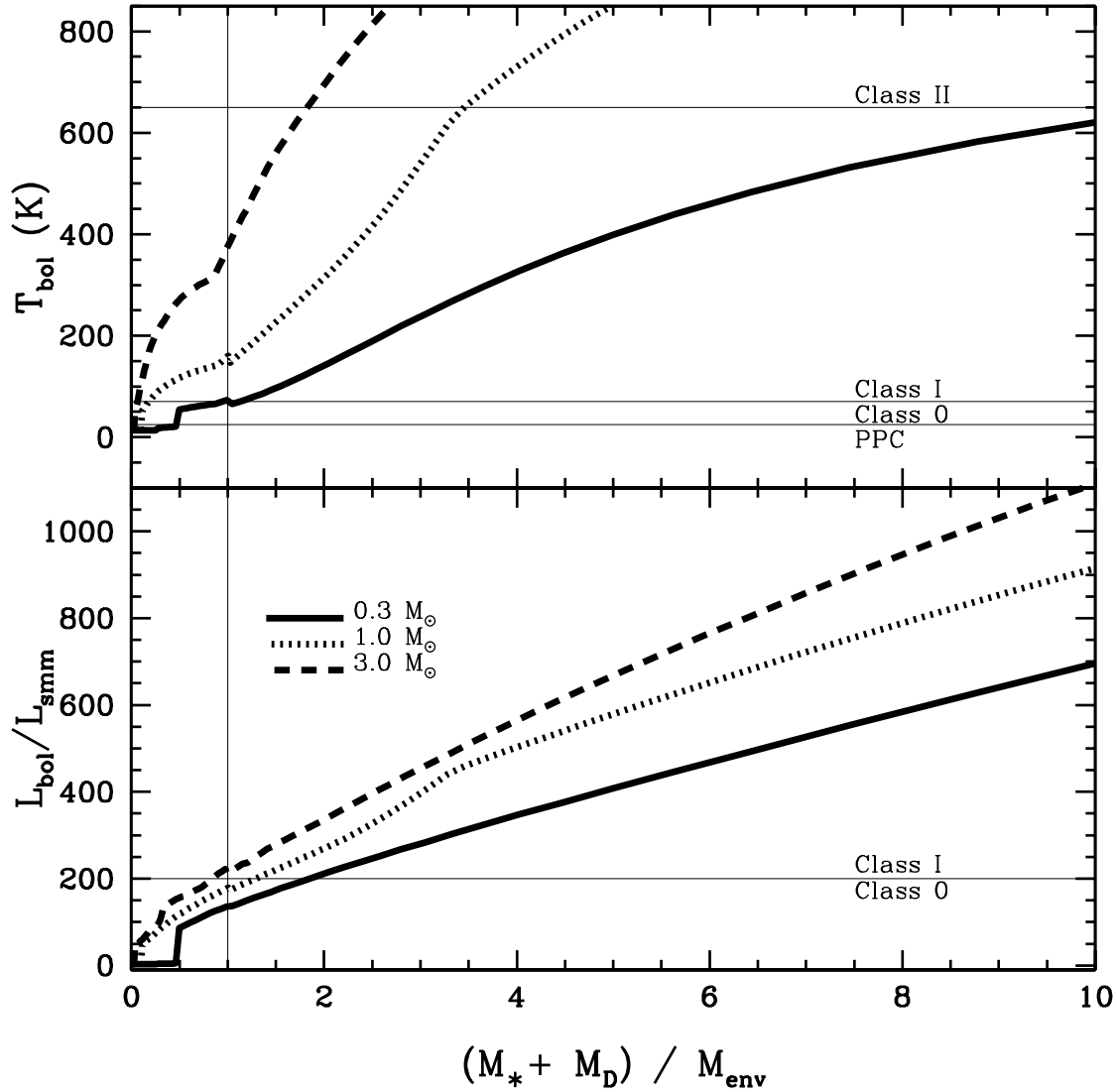


FIG. 18.— Two evolutionary signatures,  $T_{\text{bol}}$  and  $L_{\text{bol}}/L_{\text{smm}}$ , are plotted against the ratio  $(M_* + M_D)/M_{\text{env}}$ . The thin horizontal lines denote boundaries for the class transitions while vertical line marks where the star+disk mass equals the envelope mass.

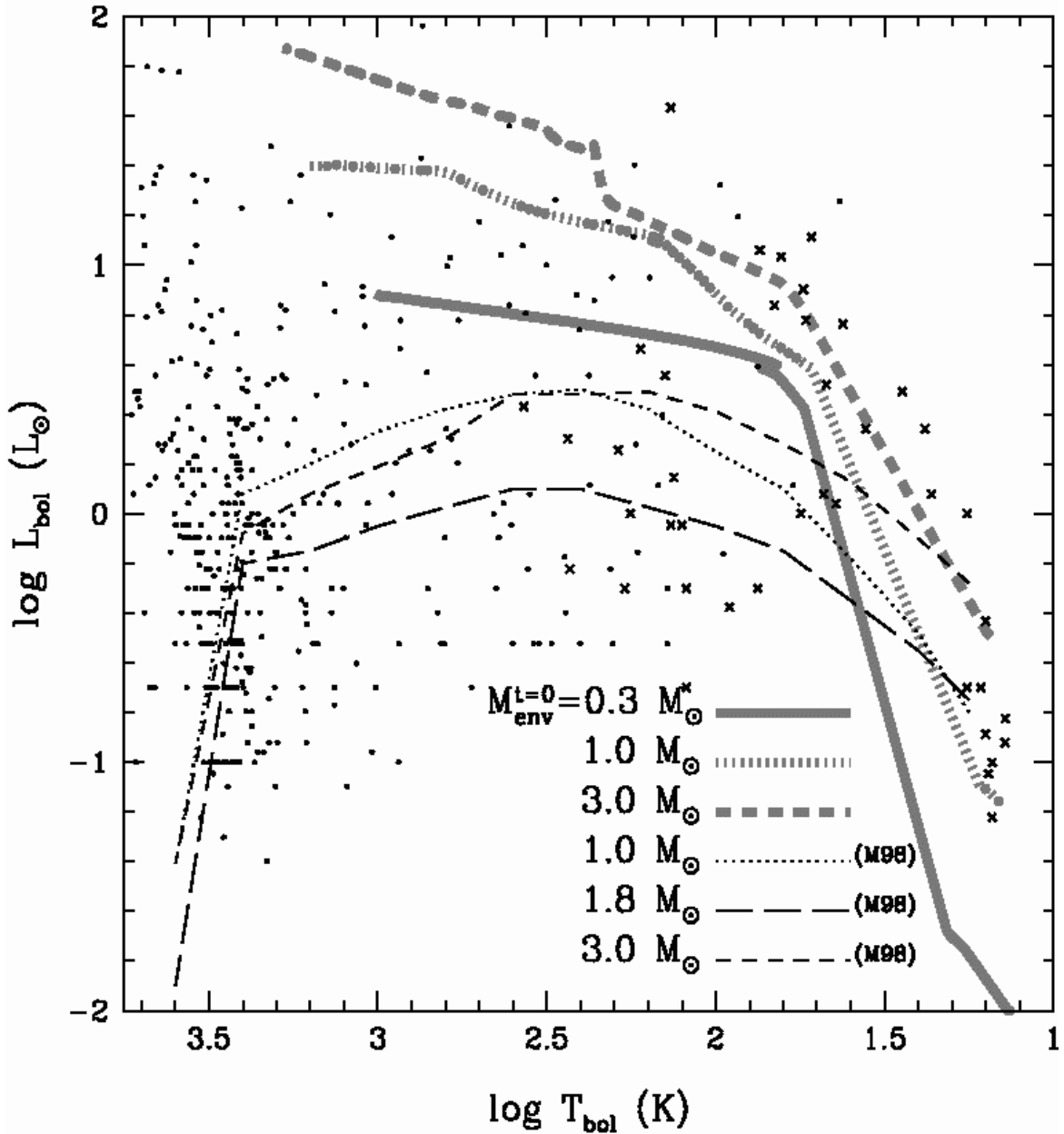


FIG. 19.— As seen in M98, this is a bolometric luminosity and temperature diagram. The thick lines are our models for three different initial masses. The thin lines are models from M98 with the initial envelope masses labeled. The  $1.0$  and  $3.0 M_{\odot}$  models are from figure 7 in M98. The  $1.8 M_{\odot}$  model is from figure 9 in M98. The crosses are from Young et al. (2003), Shirley et al. (2002), and Shirley et al. (2004). The dots are from Chen et al. (1995) and Chen et al. (1997).

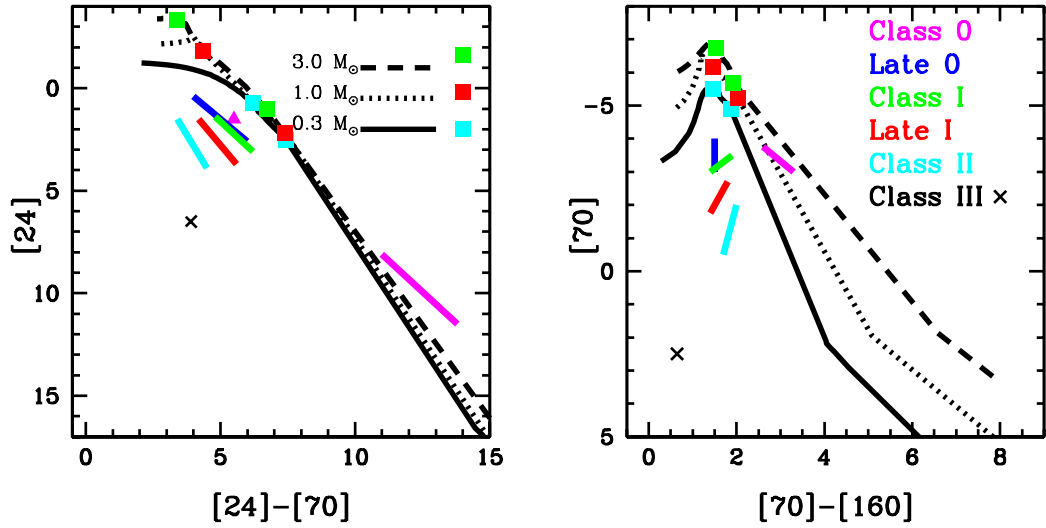


FIG. 20.— The black lines in this plot represent the SST MIPS colors as calculated for our models; [24], [70], and [160] are the magnitudes observed with MIPS. The colored lines are from Whitney et al. (2003) and extend over varying inclination angles. For the Class 0 models, the line represents most inclination angles except for the pole-on scenario, which is shown here as a magenta, filled triangle. Transitions, as discussed in Section 7.4, for the  $1 M_{\odot}$  models are shown as red squares while the green squares represent the transitions for the  $3 M_{\odot}$  model and cyan for the  $0.3 M_{\odot}$  core.